

## TOPICAL REVIEW

# Measurement and interpretation of elastic and viscoelastic properties with the atomic force microscope

**Phil Attard**

School of Chemistry F11, University of Sydney, NSW 2006, Australia

Received 23 September 2007

Published 1 November 2007

Online at [stacks.iop.org/JPhysCM/19/473201](http://stacks.iop.org/JPhysCM/19/473201)

## Abstract

This review focuses upon the measurement of force, indentation, and deformation with the atomic force microscope (AFM). Measurement and theory for elastic and viscoelastic particles and substrates are covered, as well as for deformable fluid drops and bubbles. A brief review is given of papers that use tapping mode imaging, normal and lateral force modulation, noise spectra, and indentation measurements. Measurement and calibration techniques that are essential for quantitative results with the AFM are discussed in detail. The author's contribution to elastic and viscoelastic theory for extended range forces is outlined, and the application of these to measured data for the adhesive van der Waals force and for the electric double layer repulsion is described.

## Contents

1. Introduction	2
1.1. Motivation	2
1.2. Techniques and examples	2
1.3. Preview	5
2. Measurement and calibration techniques	5
2.1. Photodiode calibration	5
2.2. Zero of separation	8
2.3. Hysteresis and velocity dependence	12
2.4. Finite thickness effects	15
3. Calculated and measured results	16
3.1. Non-contact deformation theory	16
3.2. Attraction and adhesion	18
3.3. Repulsive interaction	21
3.4. Viscoelastic measurements	25
4. Conclusion	29
Acknowledgment	30
References	30

## 1. Introduction

### 1.1. Motivation

Viscoelasticity is that phenomenon wherein the deformation of a material depends upon the previous changes in the load. It combines elastic deformation, which is determined by the current value of the load, and viscous flow, which occurs in incompressible liquids in response to pressure gradients. Viscoelastic behavior is important for biological tissues, cells, and sub-cellular structures, for industrial adhesives and gels, for membranes and surface coatings, and for polymeric materials. Polymer melts and solutions are non-Newtonian fluids and their viscoelasticity is exploited industrially in thickeners, flow improvers, and stabilizers.

A viscoelastic material has a finite relaxation time. It continues to creep for some time after the applied load has stopped changing, and it takes time for the material to recover its original shape after the load has been removed. Plastic materials, and liquid-like viscoelastic materials, never fully recover. Viscous deformation, unlike elastic deformation, is a dissipative process, which is to say that the energy expended in causing the deformation is not fully recovered during the relaxation.

These two signatures of viscoelasticity are manifest in different types of measurements with the atomic force microscope (AFM). Viscoelastic relaxation can be measured in an indentation or force measurement, by monitoring the cantilever movement following a step change in the piezo-drive. Energy dissipation can be measured from the hysteresis between the loading and unloading branches of a force measurement. Of course the piezo-drive itself usually displays creep and hysteresis, and friction due to the cantilever sliding on the substrate also causes hysteresis, so these have to be eliminated for an unambiguous interpretation. The phase difference between drive and response in an oscillatory measurement (e.g. tapping mode imaging or force modulation) can also signify viscoelasticity. Again, however, care must be taken in leaping to such a conclusion because phase differences can also be caused by a purely elastic substrate, piezo-drive inertia, or electronic delays. Phase changes during imaging can qualitatively indicate local regions of the surface with differing elasticity or viscoelasticity, but it can be difficult to quantify these in terms of material properties.

The advantage of using the AFM to measure viscoelastic properties is that it is localized, it is surface sensitive, and it yields information in molecular detail. Macroscopic rheological measurements give the bulk material behavior, but, in the case of composite materials, for example, they cannot give directly the individual properties of the matrix, or of the inclusions or their interfaces, which could be crucial information required in designing new materials. Similarly, the different components of a biological cell have differing material properties, and the measurement of these individually can be important for understanding their function and ultimately to altering, controlling, or otherwise exploiting them. Surface sensitivity is important because, for example, the structure of a polymer is different at the surface from the bulk, and consequently the response of the surface layers to stress is also different. This can be probed with the AFM in a way that bulk rheometry cannot. Although surface properties are its forte, the AFM can also measure bulk viscoelastic properties, such as those of non-Newtonian fluids like polymer melts or solutions, which approach bulk values as the separation between the probe and the substrate is increased. The advantage of the AFM over macroscopic rheometry in this case is its molecular resolution. Such molecular detail, both for bulk and for surface measurements, is ideal for testing and developing theories of viscoelasticity, and for designing nanomaterials and devices.

### 1.2. Techniques and examples

The AFM has been used on a range of systems to measure quantitatively or qualitatively viscoelastic properties. Perhaps the most common type of study is tapping mode imaging,

where the phase information is used to deduce local dissipation due to viscoelastic behavior. A number of such studies have been performed, and examples include polymeric surfaces [1–15], non-Newtonian fluids [16, 17], and biological cells and sub-structures [18–21].

Related to tapping mode imaging is the force modulation technique, where the cantilever is oscillated at fixed or slowly varying load, and the amplitude and the phase angle are measured without lateral scanning. In the force modulation method results are obtained as a function of the tip–sample distance for fixed drive frequency [22, 23], whereas in the frequency-sweep method the drive frequency is varied at a fixed distance [4, 24, 25]. As examples, force modulation has been used to characterize biological samples [26–29] and polymeric surfaces [8, 30–34]. The elastic modulus of polymer nanotubes has been determined by a modulation technique [35].

In the context of tapping mode imaging and of force modulation, it is important to note the warning of Friedenbergh and Mate [30], who cautioned against interpreting the in-phase and out-of-phase responses of force modulation microscopy as simply ‘elasticity’ and ‘viscosity’. A number of researchers have modeled the tapping process in an attempt to quantitatively extract the viscoelastic properties from the images [13, 15, 32, 33, 36–39]. If nothing else these studies confirm that the phase lead or lag is not simply related to the viscoelastic moduli of the sample.

Instead of force modulation, lateral modulation has been used, and lateral friction curves have been measured in an attempt to obtain the friction coefficient and also the viscoelastic moduli [40–43]. Basire and Frétigny [44] studied the lateral force in the stiction regime for styrene-butadiene, and found that it increased with dwell time prior to the measurement, in correlation with an increase in indentation during this time using indentation and force measurements; they [45] also found that the lateral friction force increased during the relaxation following a step change in the normal load.

A different approach has been advocated by Johannsmann and co-workers [46–50], who measured the thermal spectra of the cantilever noise. In conjunction with a Langevin equation and the fluctuation–dissipation theorem, this gives a type of friction coefficient and an effective spring constant as a function of distance from ‘contact’. Whilst these presumably correlate with the viscoelastic properties of the substrate and liquid interlayer, it is unclear how to obtain quantitatively the viscoelastic modulus or creep compliance function of the material from the data.

From the quantitative perspective, perhaps the most promising approach to the determination of viscoelastic moduli with the AFM is force measurement. This may also be called indentation, with the word used in the widest sense to include contact and non-contact deformation, and also elastic deformation. In macroscopic measurement, indentation refers exclusively to contact, and generally to permanent or plastic deformation. In the AFM it is not possible to unambiguously define ‘contact’, and in the viscoelastic case indentation describes a penetration or deformation that relaxes after removal of the force. In the present review the measurement of the adhesion or maximum pull-off force will also be considered as a force measurement. As mentioned above, in force measurement the signature of viscoelasticity is hysteresis between the loading and unloading branches, and also time and velocity dependence of the results.

Although viscoelastic force measurements have been performed on a range of biological materials [51–58], arguably the quantitative modeling of AFM measurements is more straightforward for homogeneous polymeric substrates or particles [59, 60]. The most common approach to the analysis of the force measurements is to modify the classical elastic theories of contact mechanics, such as Hertz for non-adhesive surfaces and Johnson–Kendall–Roberts (JKR) for the case of adhesion [61]. In general either a time-dependent Young’s modulus, also known as the creep compliance function, or else a time-dependent surface energy is introduced. In the opinion of the present author, the latter approach has no physical basis.

The creep compliance function rests on sound physical principles, but some caution should be exercised where a phenomenological relationship is invoked for this. In many cases it is simply inserted into Hertz or JKR theory, which, as argued below, is not correct since these theories are predicated on a static free energy minimization procedure that does not apply to time-varying deformation of viscoelastic materials.

Examples of the modified contact mechanics approach include the work of Chizhik, Tsukruk and co-workers [62–66], who performed force measurements on various polymeric substrates and measured a rate dependence. They discussed the data in terms of a Hertz-type theory due to Johnson [67] that says that the cube of the contact area is proportional to the rate of loading and to the creep compliance function. Mahaffy *et al* [20, 21] modified the Hertz model for elastic deformation by doing a Taylor expansion for a small oscillatory deformation due to an oscillatory perturbing force, with the coefficient connecting these defined as a viscoelastic material parameter whose real part is said to reflect the elastic storage response, and whose imaginary part is said to reflect the viscous loss response of the sample. (As mentioned above, such an interpretation of the phase difference is not correct [13, 15, 30, 32, 36–39].) Vakarelski *et al* [68] measured time- and velocity-dependent adhesions, and described their data with JKR theory and a fitted, time-dependent surface energy. Opdahl *et al* [69] used AFM force measurements to characterize changes in the surface viscoelastic and adhesive properties of bulk hydrated and dehydrated poly(hydroxyethyl) methacrylate-based contact lenses as a function of humidity, taking the Young's modulus from a fit to the elastic Hertz theory. Yang *et al* [70] measured force hysteresis in glassy polymer films, and they were able to describe the loading branch alone with a spring and dashpot model of the surface combined with a phenomenological model of the time rate of change of the viscoelastic material parameters and JKR theory. Mary *et al* [71] developed a JKR-type contact theory for adhesive layered substrates indented by a sphere. The analysis, which extended earlier work [72–74], was applied to macroscopic indentation measurements of a glass lens and a cross-linked acrylate polymer, and has also been used for lateral loading [75].

Contact mechanics is appropriate for macroscopic measurements, where the deformations and contact areas are large on molecular length scales. For the AFM, however, the measurements are carried out with molecular resolution, the probes are colloidal sized, and the size of deformations, separations, and contact areas are comparable to the range of the surface forces that are involved. In realistic cases, charged surfaces in an electrolyte can interact via an electrical double layer repulsion that decays over length scales of 1–100 nm, and the van der Waals attraction that arises between all bodies has a measurable range of 1–10 nm. Such extended ranges create conceptual difficulties in defining what is meant by contact, and even if some operational definition of contact and non-contact could be agreed, the surfaces beyond the contact region still interact across the gap. Such effects are ignored in contact theories, and so in general they are not capable of quantitatively describing AFM measurements with the resolution that the device is capable of.

In the case of viscoelastic materials there is an additional reason for going beyond contact theories. The functional forms that are the Hertz and the JKR theories for repulsive and for adhesive surfaces, respectively, result from the minimization of the elastic and surface energies, and that due to the applied load. This is an equilibrium result and it is valid only in the static case for elastic materials. There is no such minimization principle for non-equilibrium systems, and in the viscoelastic case with time-dependent loads and deformations these functional forms are simply not applicable, even if the contact picture were. One cannot simply insert a creep compliance function into Hertz or JKR theory and apply them to viscoelastic deformation.

Arguably the only viable approach is to combine the fundamental equations of elasticity with the actual surface forces present, and to solve the resultant system of equations

numerically. What one loses compared to Hertz or JKR theory is analytic approximation (except for elastic deformation where some accurate approximations for extended range forces have been obtained) [76]. What one gains is the certainty of an approximation-free theory that is soundly based on the accepted equations of elasticity and viscoelasticity and on the known surface forces.

The present author has developed algorithms for the treatment of deformation due to realistic forces of extended range, and has given results in both elastic [76, 77] and viscoelastic [78, 79] cases. In the elastic case the theory has been applied to model measured data for the case of attractive van der Waals forces [80], repulsive electrical double layer forces [81], and oscillatory solvation forces [77, 82]. In the viscoelastic case adhesive surfaces that interact with van der Waals attractions have been modeled [79], as have charged surfaces that interact with an electrical double layer repulsion [78], and the latter has been applied quantitatively to actual AFM data [83, 84]. The case of AFM force measurements of bubbles, vesicles, and droplets, whose deformation is due to membrane elasticity, has also been studied by the present author [85, 86].

### *1.3. Preview*

This review focuses on two main areas in which the author has contributed to the measurement of elastic and viscoelastic materials with the AFM. In section 2 the actual technique of force measurement with the AFM when the surfaces are deformable is described. It turns out that for deformable substrates or probes one cannot use the same methods to calibrate the AFM or to analyze the force curves as one does for rigid surfaces. In view of the fact that a significant proportion of papers in this field, including many cited above, have not carried out the appropriate calibration or analysis, it seems worthwhile to review the correct experimental techniques in detail.

In section 3 measured and calculated data are given for deformable surfaces. As mentioned at the end of the preceding sub-section, the best suited theoretical approach to deformation measured with the AFM is one that accounts for the extended range of the surface forces, and both the computational algorithm and model results obtained by the author are reviewed below. These ought be useful as an indication of what is to be expected for an AFM measurement in the elastic or in the viscoelastic case, and they should aid the design of measurement protocols and the qualitative interpretation and quantitative analysis of data.

## **2. Measurement and calibration techniques**

### *2.1. Photodiode calibration*

The measurement of forces and the quantitative extraction of material properties with the AFM requires certain instrumental calibrations. The first and most important of these is the photodiode sensitivity, which converts the measured voltage to cantilever deflection and thence to force via the cantilever spring constant, which must be independently measured. For rigid substrates, the standard method is to take the slope of the constant compliance region (change in voltage divided by change in piezo-position) as the sensitivity factor, since one can be assured that movement of the substrate is rigidly translated into deflection of the cantilever [87]. The spring constant can be determined by resonance methods [88, 89] or by calculation [90].

Figure 1 shows AFM force data obtained for a silica substrate partially covered with patches of polystyrene film [91]. In figure 1(A), one can see the photodiode saturation at  $\pm 10$  V, and, at negative voltages, the horizontal, zero force regions. The measurements were obtained

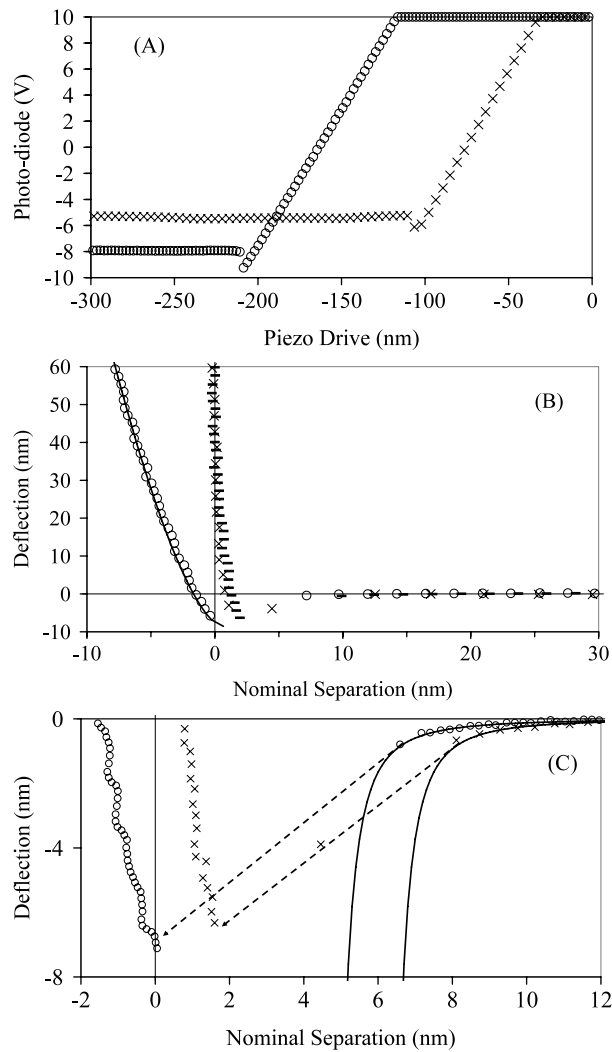


**Figure 1.** Deflection of an AFM cantilever (spring constant  $k = 0.58 \text{ N m}^{-1}$ ) for a tip in air approaching a rigid silica substrate (crosses) and a polystyrene film (circles and dashes). (A) Raw photodiode voltage versus piezo-crystal extension. The two data series are offset for clarity. Note the difference in slopes of the constant compliance contact regions. (B) Cantilever deflection versus nominal separation. The calibration factor was obtained from the slope of the constant compliance region of silica (circles and crosses) or from that of polystyrene (dashes). The post-contact deformation (negative separations) for polystyrene has been fitted with JKR theory (obscured curve) using  $E/(1 - \nu^2) = 1 \times 10^8 \text{ Pa}$ , a radius of curvature  $R = 700 \text{ nm}$ , and a fitted surface energy,  $\gamma = 1.5 \text{ mJ m}^{-2}$ . (C) The jump into contact fitted with the van der Waals attraction. The water-air-water Hamaker constant,  $A = 3.7 \times 10^{-20} \text{ J}$ , was used, and a fitted  $R = 700 \text{ nm}$ , and a fitted  $d = 4.5 \text{ nm}$  for polystyrene and  $d = 6 \text{ nm}$  for silica. Data from [91].

by bringing the tip into contact on either the bare silica or on a polystyrene patch, without changing the set-up of the AFM. This means that the change in slope in figure 1(A) is due to the deformation of the polystyrene. The slope of the constant compliance region for rigid materials gives the calibration factor for the photodiode, which is also called the sensitivity. From the silica data, this is  $0.23 \text{ V nm}^{-1}$ . The polystyrene data have a lower slope,  $0.21 \text{ V nm}^{-1}$ , which

is due to the fact that only part of the motion of the piezo-drive goes into moving the tip of the cantilever; the rest goes into indenting the polystyrene.

The sensitivity factor is used to convert the photodiode voltage to cantilever deflection,  $x$ . Multiplying the latter by the spring constant gives the force or applied load,  $F = kx$ . The nominal separation is the actual separation between the surfaces if they are completely rigid. It is the deflection minus the drive distance,  $h_0 = x - z + \text{const.}$ , using a suitable sign convention. The constant represents the choice of the zero of separation. For rigid surfaces the separation cannot be negative, and so zero corresponds to the position where the force curve becomes vertical. For deformable surfaces the choice of zero is more problematic (see below), and in figure 1 for polystyrene it was fixed at the position following the van der Waals jump. Negative values of the nominal separation correspond to the amount of deformation that has occurred. This is also called flattening, indentation, or penetration.

The point of the dashed polystyrene data in figure 1(B) is to show what goes wrong if the slope measured for a deformable surface is used to calibrate the photodiode. In this case the magnitude of the force is wrong, the separation prior to contact is wrong, and the indentation post-contact is completely neglected. Note that the polystyrene data look quite linear at larger loads. Hence one cannot conclude from the linearity of the constant compliance region that the surfaces are undeformable. This erroneous procedure—using the high load, apparently linear part of the force curve for a deformable surface to calibrate the photodiode—is quite common in the literature. Unless a paper specifies the actual method of calibration explicitly, it should be assumed that the erroneous procedure was used and the results should be regarded as qualitative rather than quantitative.

The lesson is that if the sensitivity of the photodiode is measured by a contact method (a non-contact method will be discussed shortly) then it must be obtained with rigid substrates and probes. In the present case a patchy deformable film was used, so that the calibration against the bare silica could be performed in the same experiment as the actual measurement of the deformation merely by shifting the point of contact. This technique can also be used if one has a deformable colloidal probe mounted on a rigid substrate (and a rigid tip or probe on the cantilever). In the case that the entire substrate is deformable, it may be possible to perform the calibration by placing a rigid cover slip on top of the substrate. Deformation of the underlayer will then be negligible since it is proportional to the local pressure, which is minimized by the rigid cover slip. Alternatively, an *ex situ* calibration may be performed by exchanging the substrate for a rigid one, taking care not to alter the set-up of the AFM, as can be done with practice [92]. One ought to confirm the reproducibility of such an *ex situ* calibration by repetition.

The polystyrene film of figure 1 showed little hysteresis between loading and unloading, and so it was taken to be elastic and the deformation following the jump into contact in figure 1(B) was fitted with the JKR theory [61]. The fitted value of the elasticity parameter,  $E/(1 - \nu^2) = 1 \times 10^8$  Pa, depends on the value of the tip radius, but the latter is constrained by physically reasonable values of the Hamaker constant because the product  $AR$  must be constant to fit the van der Waals force. The lower bound, which was used here, corresponds to the water–air–water value  $A = 3.7 \times 10^{-20}$  J [93], which gives  $R = 700$  nm and  $E/(1 - \nu^2) = 0.1$  GPa. The upper bound corresponds to the silica–air–silica value  $A = 7 \times 10^{-20}$  J [93], which gives  $R = 350$  nm and  $E/(1 - \nu^2) = 0.15$  GPa. The value 0.1 GPa is markedly less than the value of bulk polystyrene,  $E = 3$  GPa [94], and is consistent with the fact that the surface of polystyrene films is less glassy than the bulk [95–100]. Overney *et al* [16] also estimated a value of 0.1 GPa using the AFM.

Figure 1(C) shows the jump into contact due to the van der Waals attraction. The extended range of the surface force is graphically illustrated here. The data have been fitted for a force of

the form  $F(h) = AR/12(h - d)^2$ , where  $h$  is the surface separation,  $A$  is Hamaker constant,  $R$  is the radius of curvature of the tip, and  $d$  is the total thickness of any water films on the surfaces. The evidence for the water film is the hook at the base of the constant compliance data for silica, which is due to the finite time it takes to drain the water from the contact region. The water film arises from the humid atmosphere and it is thicker on the more hydrophilic surface. (The value for polystyrene may in fact represent a film on the silicon nitride cantilever tip.)

*2.1.1. Non-contact photodiode calibration.* If the spring constant of the cantilever is known, then it is possible to calibrate the photodiode from the thermal fluctuations in the voltage [101]. Fitting a Lorentzian to the noise spectrum of the fundamental mode (i.e. the first peak of the thermal spectrum), one can obtain the resonance frequency  $f_R$  in hertz, the dc power response  $P_{dc}$  in  $V^2 \text{ Hz}^{-1}$ , and the quality factor  $Q$  [102]. It must be emphasized that these are fits to the fundamental mode. In terms of these the calibration factor for the cantilever is [101]

$$\alpha = 1.2771 \sqrt{\frac{3\pi k f_R P_{dc} Q}{8k_B T}}, \quad (2.1)$$

where  $k$  is the spring constant,  $k_B = 1.38 \times 10^{-23} \text{ J K}^{-1}$  is the Boltzmann constant, and  $T$  is the absolute temperature. The pre-factor 1.2771 arises from the conversion from angular deflection to position deflection, and from the ratio of the power in the first mode to the total power. In SI units  $\alpha$  is in  $V \text{ m}^{-1}$ , and corresponds to the slope of the constant compliance curve for rigid surfaces discussed above. With it, the deflection of the cantilever is  $x = \Delta V / \alpha$ , and the force is  $F = kx$ . A more detailed discussion of this result, and a correction for the tilt of the cantilever and for friction, is given in [101].

The above result requires the spring constant of the cantilever, which can be obtained in a prior experiment by the usual thermal method [103–105] or by attaching a mass to the cantilever and measuring the resonance frequency [88]. Care ought to be taken to place the mass precisely at the place where the tip or the probe joins the cantilever because the effective spring constant scales with the cube of the free length of the cantilever, and a small discrepancy in the position used to measure the surface force and that used to measure the gravitational force gives a large error in the effective spring constant. Similarly, the spring constant measured by the thermal method should be increased by a factor of  $(L_0/L_1)^3$ , where  $L_0$  is the total length of the cantilever, which gives the thermal resonance, and  $L_1$  is the distance where the base joins the tip, or to where the colloid probe will be attached, as this is the distance that gives the measured force.

This *in situ* non-contact calibration method is the preferred calibration method, even when one has the option of obtaining a rigid body constant compliance slope (because that can be vitiated by friction). The thermal method has the additional advantage of being able to be used when a deformable colloid particle is mounted on the cantilever, or when the cantilever tip is functionalized and cannot be brought into contact prior to the actual measurement.

## 2.2. Zero of separation

In macroscopic measurements the distinction between contact and non-contact is unambiguous. Within the resolution of the device all forces have zero range, and so any non-zero load means that the bodies are in contact. The situation is not so straightforward at the molecular level, since molecules interact over extended ranges, and if non-zero force were taken to mean contact then all surfaces would be in contact all the time. What is required is an operational definition of contact that can be used to compare different measurements and that can be matched with theory.

In the case of rigid bodies, such as silica in figure 1, one can choose the zero of separation to be the point where the force is vertical, which coincides with the constant compliance region whose slope was used to calibrate the photodiode. The rationale for this choice is that the range of the Fermi repulsion between molecules is much shorter than the resolution of the AFM, and it is this repulsion that is responsible for preventing the interpenetration of solid bodies. In this case the definition of contact coincides with the normal macroscopic picture.

For the case of deformable bodies the situation is more complex. In this situation one defines the nominal separation as

$$h_0 = x - z + \text{const}, \quad (2.2)$$

where  $x$  is the cantilever deflection, which is positive for a repulsion,  $z$  is the piezo-distance, which increases on approach and causes the nominal separation to decrease, and the constant is chosen so that the nominal separation becomes zero at an appropriate position, as will be shortly specified. This definition ignores deformation, and so for rigid bodies the nominal separation coincides with the actual surface separation, and the constant is chosen so that the actual surface separation is never negative.

For deformable bodies, the actual separation is the nominal separation less the deformation,

$$h = h_0 - u. \quad (2.3)$$

The geometry is sketched in figure 2. The deformation is the extension of the surfaces. An attractive force causes such an extension and a positive deformation, and in this case the actual separation is less than the nominal separation. Conversely, flattening occurs for a positive load (repulsion), in which case  $u$  is less than zero, and the actual separation is greater than the nominal separation. The nominal separation can be negative. If the zero is chosen appropriately so that  $h = 0$  corresponds in some sense to physical contact, then the negative value of the nominal separation corresponds to the amount of flattening of the surfaces. Such a picture is most appropriate for surfaces that cannot interpenetrate; for loosely packed polymeric surfaces this interpretation may not reflect reality.

For the case of the deformable polystyrene film in figure 1, the zero of nominal separation was set as the first point following the van der Waals jump into contact. This has the virtue of being well-defined and unambiguous. The amount of elastic extension of the surfaces at the end of the jump can be estimated as 0.7 nm from JKR theory [61], and at the beginning of the jump it is 0.5 nm from the central deformation approximation [76]. Hence this convention for the zero of separation gives a reasonably realistic picture of the amount of deformation that actually occurs to within about 1 nm.

For the case of an electric double layer repulsion there may not be a van der Waals jump, and so a different criterion is required to set the zero of separation. Figure 2 shows the force measured between a rigid silica colloid probe and a deformable poly(dimethylsiloxane) (PDMS) solid droplet [106]. It can be seen that the slope of the force is continuous, and that there is no clear demarcation of contact and non-contact. For rigid bodies 1 and 2 the electrical double layer force is given reasonably accurately by the renormalized linear Poisson–Boltzmann equation [107, 108]

$$\begin{aligned} F(h) &= 64\pi\epsilon_0\epsilon_r R(k_B T/q)^2 \gamma_1 \gamma_2 \kappa_D e^{-\kappa_D h} \\ &\equiv 2\pi R \kappa_D^{-1} P e^{-\kappa_D h}, \end{aligned} \quad (2.4)$$

where  $R^{-1} = R_1^{-1} + R_2^{-1}$  is the effective radius,  $\epsilon_0$  is the permittivity of free space,  $\epsilon_r$  is the relative permittivity of the solvent,  $\kappa_D^{-1}$  is the Debye length, and  $q = ze$  is the valence of the ions times the charge on a proton (a symmetric electrolyte is assumed). In plotting this expression the nominal separation is used, which will coincide with the actual

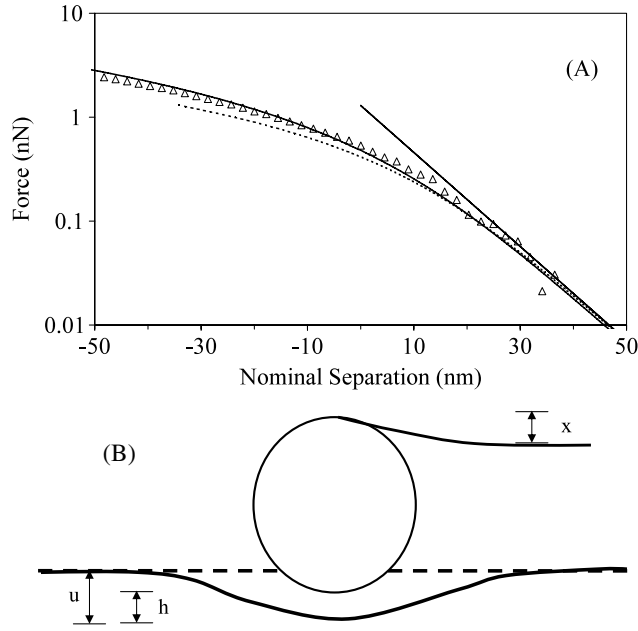


**Figure 2.** (A) AFM force measurement (triangles) for a PDMS droplet ( $\psi_1 = -46$  mV,  $R_1 = 0.6 \mu\text{m}$ ) and a silica sphere ( $\psi_2 = -70$  mV,  $R_2 = 5 \mu\text{m}$ ) in 1 mM  $\text{KNO}_3$  at pH 9.8 on approach [106]. All curves use the renormalized linear Poisson–Boltzmann law with the measured zeta potentials. The straight line is for rigid particles, the dotted curve is the analytic central deformation elastic approximation, and the solid curve is the numerical elastic calculation (with a short-range,  $1/h^9$ , steric repulsion added). Both of the curves use a fitted elasticity  $E = 0.4$  MPa. (B) Sketch of the geometry. The colloid probe (sphere) is attached to the cantilever, which deflects upward by  $x$  under the influence of a repulsive force. The surface of the undeformed substrate is represented by the dashed line, and that of the deformed substrate is represented by the solid curve. The amount of deformation is  $u < 0$ , and the separation between the actual surfaces is  $h > 0$ . The nominal separation,  $h_0 = h + u$ , is in this case negative.

surface separation at large separations (small forces) when the surfaces are undeformed. The renormalized potential is

$$\gamma = \tanh(q\psi/4k_B T), \tag{2.5}$$

where  $\psi$  is the diffuse layer potential, which may be taken to be equal to the measured zeta potential [108].

In figure 2, the zero of separation has been chosen so that the measured data coincide with the calculated rigid body force at large separations [109]. The rationale for this choice is that deformation is always negligible for weak enough forces. Of course what ‘weak enough’ means depends upon how deformable the surfaces are. Whether the AFM has the resolution to access the weak force regime is indicated by whether or not the measured data coincide with the rigid body data at large separations, as they do in figure 2.

The measured repulsion plotted against nominal separation is less for deformable bodies than for rigid bodies. That is, the measured data in figure 2 lie below the straight line, which would be the result if the surfaces were rigid. This is because at a given nominal separation the actual surface separation is greater due to flattening,  $h > h_0$ . Hence the force, which to leading order is the rigid body result evaluated at the actual surface separation, is weaker. This can be seen from the so-called central deformation approximation (CDA) [76], which gives the

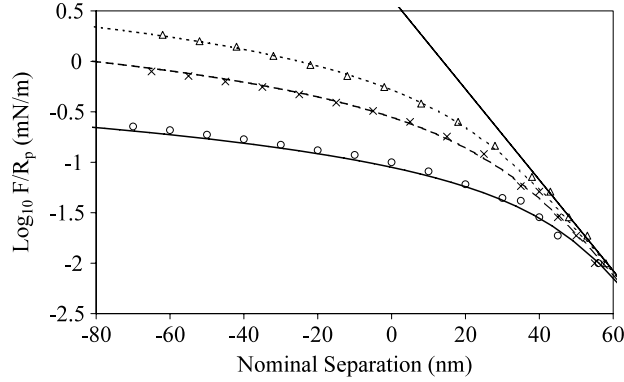


**Figure 3.** AFM data [111] for an *n*-decane oil droplet,  $R_b = 0.25$  mm and silica colloid probe  $R_p = 3$   $\mu$ m, interacting in 1 mM NaNO<sub>3</sub>,  $\kappa_D^{-1} = 9.65$  nm. From bottom to top the concentration of the added SDS surfactant is  $3 \times 10^{-1}$ ,  $10^{-3}$ , and  $10^{-5}$  M. The renormalized linear Poisson–Boltzmann law (bold line) uses the measured zeta potentials  $\psi_{\text{SiO}_2} = -70$  mV [112] and  $\psi_{\text{decane}} = -100$  mV [113]. The curves are the results of deformation calculations using a fitted interfacial spring constant [85, 86].

deformation due to the electric double layer force,

$$u = -\sqrt{\frac{8\pi R}{\kappa_D E^2}} P e^{-\kappa_D h} \equiv -\omega e^{-\kappa_D h}, \quad (2.6)$$

where  $E = E'/(1 - \nu^2)$  is the elasticity parameter. This gives the nominal separation as a function of the actual separation,  $h_0(h) = h + u(h)$ . The dotted curve in figure 2 is the rigid body  $F(h)$  versus this CDA  $h_0(h)$ . It can be seen that the CDA captures almost all of the effect of the elastic deformation. The full curve is a full numerical calculation of the elastic deformation due to the electric double layer force, and it can be taken as exact [76]. The small increase in the repulsion over the CDA is the extra work that goes into the elastic deformation of the body.

One interesting result for deformable surfaces is that the deformation renormalizes the decay length at large loads. The CDA gives the force as [110]

$$F(h_0) = 2\pi R \kappa_D^{-1} P' e^{-\kappa' h_0}, \quad (2.7)$$

where the renormalized decay length is

$$\kappa' = \frac{\kappa_D}{1 + \omega \kappa_D}, \quad (2.8)$$

and the renormalized pressure pre-factor is

$$P' = P e^{-\kappa' \omega}. \quad (2.9)$$

This result is valid in the range  $-\omega < h_0 \ll \kappa_D^{-1}$ .

Figure 3 shows results for oil droplets, which are charged due to adsorption of surfactant from solution [111]. Again the zero of separation has been set to ensure that the data coincide with the rigid body result at large separations. The curves are a result of a calculation that takes into account the deformation of the droplet as it wraps around the probe particle [85, 86]. One can conclude that even though there is no sharp demarcation of contact and non-contact for repulsive electrical double layer forces, the procedure for setting the zero of separation advocated here works quite well.

For a bubble or droplet, the wrap radius at a given force  $F$  is [85, 86]

$$R_w = R_0 \frac{F \kappa_D R_p + 4\pi \sigma R_p}{F \kappa_D R_0 - 4\pi \sigma R_p}, \quad (2.10)$$

where  $R_0$  is the original radius of the bubble or droplet,  $R_p$  is the radius of the probe, and  $\sigma$  is the surface tension. The actual surface separation (closest separation, which is on the axis) is

$$h = \kappa_D^{-1} \ln \frac{2\pi R_p R_w P}{\kappa_D F [R_w - R_p]}. \quad (2.11)$$

Unlike a solid elastic body, the bubble or droplet behaves like a Hookean spring, and the deformation is

$$u = -F/k_{\text{int}}, \quad (2.12)$$

with the interfacial spring constant (for a contact angle of  $90^\circ$ ) being given by [114]

$$k_{\text{int}}^{-1} = \frac{-1}{4\pi\sigma} \ln \frac{R_p}{2\kappa_D R_0^2}. \quad (2.13)$$

The nominal separation is of course  $h_0 = h(F) + u(F)$ , which gives the curves in figure 3.

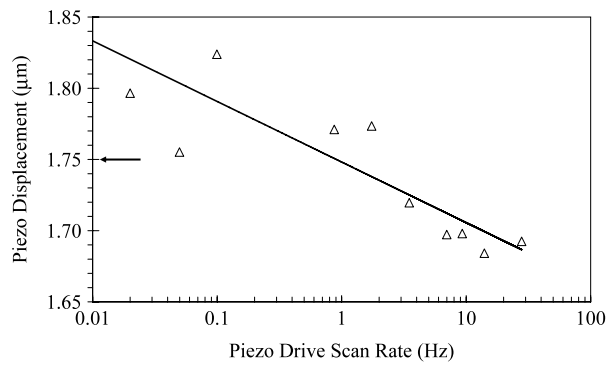
From these last two figures and the associated analysis one can conclude that elastic solids and fluid droplets behave differently under loads. Whereas an elastic solid has a non-linear deformation as a function of load, and a renormalized decay length under high loads, the deformation of a fluid droplet is perfectly linear with load. What both deformable objects have in common is that the measured force as a function of nominal separation is less than that between rigid bodies due the fact that flattening increases the actual surface separation. Plotted against actual surface separation the force would be larger due to the extra energy that goes into elastic and interfacial deformation. What they also have in common is that at large separations or weak forces, they both behave as rigid bodies, which fact should be used to set the zero of separation.

### 2.3. Hysteresis and velocity dependence

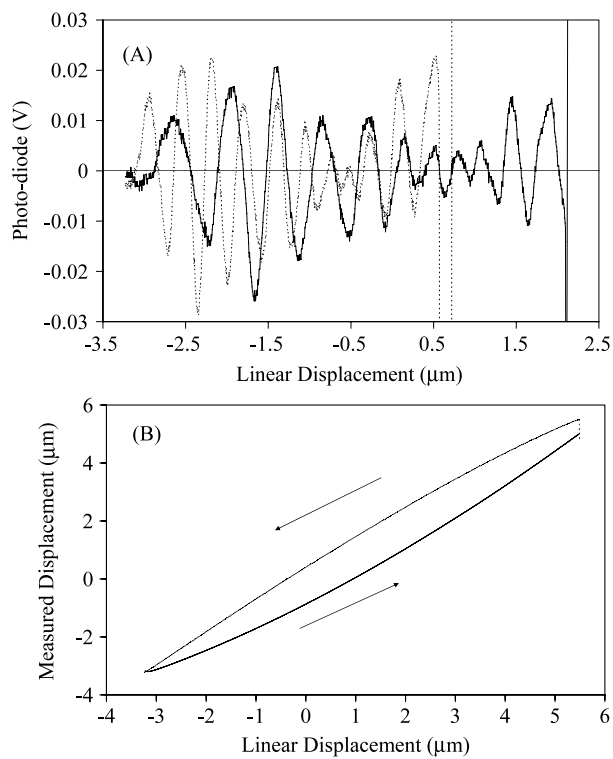
As discussed in section 1, viscoelastic materials are characterized by their finite relaxation time, which leads to velocity dependence, hysteresis, and other time-dependent effects. In seeking to quantify these by measurement with the AFM, it is essential that other time-dependent contributions be either eliminated or at least estimated. Unfortunately, piezo-crystals that are used to change the sample–probe separation display non-linearities, hysteresis, and velocity dependence that must be accounted for.

Figure 4 shows that the expansion factor of an AFM piezo-drive is indeed velocity dependent [84, 91]. The data were obtained by applying a sinusoidally varying voltage to the piezo-drive and directly measuring the amplitude of the piezo-drive response. The amplitude of the applied voltage was fixed as the frequency was varied. Hence the figure is equivalent to measuring the velocity dependence of the piezo-crystal expansion factor. In the context of a viscoelastic measurement, where one might seek to determine the rate dependence of the deformation, for example, the velocity dependence of the piezo-crystal should be either eliminated or else measured and included in the data analysis. The 10% variation in the total expansion may seem small over the several orders of magnitude in speed. But in realistic cases one might be measuring a viscoelastic indentation that is a small fraction of the total piezo-displacement, and that can therefore be comparable to the variation shown in figure 4.

Figure 5(A) shows interference fringes that were observed on the baseline (zero force) region of an extend and retract measurement [116]. The fringes arise from interference between



**Figure 4.** Displacement amplitude of the piezo-crystal as a function of frequency of the applied voltage. The arrow indicates the displacement expected from the original interferometric calibration of the crystal, and the line is a least squares fit [91].



**Figure 5.** Hysteresis of the piezo-drive [116]. The linear displacement is the change in the applied voltage times the expansion factor. (A) Interference fringes detected by the photodiode in the base line at large separations for piezo-crystal expansion (solid) and retraction (dotted). (B) Measured piezo-crystal displacement for expansion and retraction.

the primary laser beam, which is reflected off the back of the tilted cantilever to the photodiode, and the secondary beam, which is reflected off the back of the tilted cantilever, then off the upper horizontal surface of the cell, then off the lower horizontal surface of the substrate, and thence to the photodiode. The interference from the secondary beam, which may also be due

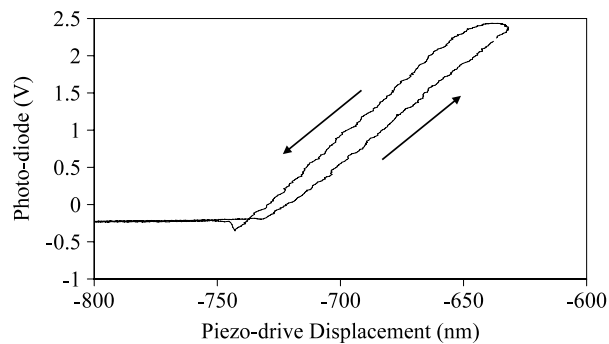


**Figure 6.** Cantilever deflection versus measured piezo-drive displacement for extend and retract for a silica colloid probe ( $R = 18 \mu\text{m}$ ) and a mica substrate in 0.1 mM NaCl. The hysteresis in the constant compliance region is due to sliding friction [117, 118].

to the reflections in the reverse order, can be eliminated by appropriate tilting of one or other of the horizontal surfaces. The point of the figure is that the interference fringes for extend and retrace do not coincide, which indicates that the piezo-drive has, at a given voltage, a different displacement on the two branches. (The abscissa for the plot was obtained from the AFM data file, and on both branches it is simply the applied voltage times the expansion factor.) This may be seen directly from the hysteresis loop in figure 5(B). Here the piezo-displacement was measured directly and plotted against the applied voltage times the expansion factor. For a given applied voltage, the discrepancy between the piezo-displacement on the two branches can be of the order of a micrometer. Such hysteresis and non-linearity are a general feature of piezo-crystals.

There are several solutions to the problem. Some manufacturers have built into the AFM a displacement sensor, and this gives the actual piezo-movement rather than the nominal movement that assumes a fixed expansion factor. There are cost-effective methods for adding such capabilities to existing devices [84]. Several AFMs operate in so-called closed-loop mode, which is to say that the piezo-displacement is measured and used to fine-tune the nominal voltage to obtain the desired piezo-displacement in real time. This can be useful for constant velocity loading or unloading, as is required to measure true material viscoelastic hysteresis, or if measurements at fixed indentation for different velocities are sought. Pre-programmed polynomial curves built in to the software of the AFM are generally not adequate.

An additional cause of hysteresis is shown in figure 6, where friction as the probe slides on the substrate in the axial direction creates a difference between the loading and the unloading constant compliance slopes [115–118]. The sliding occurs during a normal force measurement because the cantilever is tilted by about  $10^\circ$ – $15^\circ$  to the horizontal, and this causes horizontal motion along the long axis of the cantilever that can be 50–100% of the vertical piezo-extension [117, 118]. The friction due to this sliding creates a torque and an additional angular deflection on the cantilever that is equal and opposite on loading and unloading, which gives rise to the hysteresis shown in figure 6. For rigid materials, the difference in slopes can be used to measure the friction coefficient without any additional calibration being required [118]. For viscoelastic materials, disentangling the hysteresis due to sliding friction from that due to the material's viscoelasticity can be problematic. In many cases the viscoelastic hysteresis can be dominant, such as for very deformable surfaces that remain separated from actual contact due to repulsive forces. In other cases one may be able to estimate the friction coefficient (e.g. from a lateral friction measurement) [81, 92] and remove the effect of friction from the measured

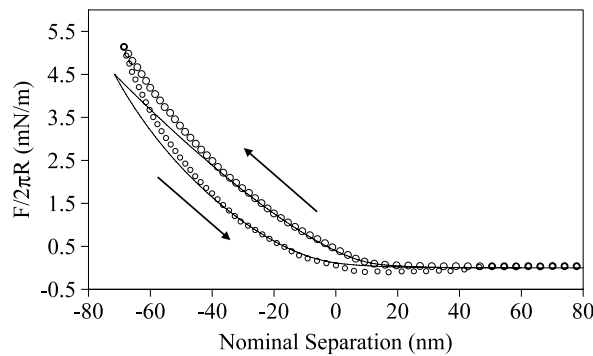


**Figure 7.** Loading and unloading force versus nominal separation for a PDMS droplet ( $R = 0.3 \mu\text{m}$ ) and a silica colloid probe in  $1 \text{ mM KNO}_3$  at  $1 \mu\text{m s}^{-1}$ . The symbols are AFM data [106] and the curve is a fit to a viscoelastic theory [78].

forces [117, 118]. These corrections remain to be investigated in detail, but one should at least be aware of this possible contribution to any measured hysteresis.

There is an additional possible cause of hysteresis in the AFM, namely that due to hydrodynamic drainage. For the usual surface forces, such as van der Waals or electric double layer, the force is the same on approach as on separation, and they are independent of velocity. They can be quantified using equilibrium theory. However, at high velocities the drainage force, which is repulsive on approach and attractive upon separation, can have a measurable effect, particularly for large colloid probes, weak cantilevers, highly viscous fluids, and close separations. In normal AFM force measurements this hysteresis is negligible.

#### 2.4. Finite thickness effects

Figure 7 shows a force or indentation measurement for a viscoelastic PDMS droplet [106]. The hysteresis between loading and unloading is clearly visible. In this case the contribution from friction has been taken to be negligible, partly because the forces are repulsive, partly because the loading branch lies above the unloading branch, which is opposite to the order caused by axial friction in figure 6, partly because the curvature of the contact region signifies that elastic effects are dominant, and partly because the hysteresis is velocity dependent (not shown) whereas the frictional hysteresis is rather insensitive to velocity [81, 92, 117, 118]. The curve in figure 7 is a fit to a non-contact viscoelastic theory [78] that will be discussed in greater detail in the following section. The relevance of this theory in the present context is not so much where the theory fits, but more the region where it does not. In the high load region, it can be seen that the force increases more rapidly with decreasing separation than is predicted by the theory that has been fitted to these and other low load data (not shown). The theory is for an infinitely thick viscoelastic solid, whereas in the measurements the PDMS solid droplet has a diameter of  $0.6 \mu\text{m}$ . It can be seen that at the highest loads the deformation or flattening, which is given by negative values of the nominal separation, is of the order of 60–80 nm, or about 10% of the thickness of the material. In these circumstances the increase in the effective stiffness seen in the measurements must be attributed to the influence of the underlying rigid substrate. Figure 7 graphically illustrates that deformations of several per cent are sufficient to be measurably affected by the finite thickness of the sample.

### 3. Calculated and measured results

#### 3.1. Non-contact deformation theory

*3.1.1. Elastic theory.* This section shows how the deformation of elastic and viscoelastic bodies may be calculated for realistic forces of extended range. The aim is to describe quantitatively the molecular level measurements made with the AFM. The theory is based upon continuum linear elasticity theory in the semi-infinite half-space approximation [119]

$$u(r) = \frac{-2}{\pi E} \int ds \frac{p_1(s)}{|\mathbf{r} - \mathbf{s}|}. \quad (3.1)$$

Here the elasticity parameter  $E$  is given in terms of the Young's moduli  $E_i$  and Poisson's ratios  $\nu_i$  of the two bodies,  $2/E = (1 - \nu_1^2)/E_1 + (1 - \nu_2^2)/E_2$ ,  $r = |\mathbf{r}|$  and  $s = |\mathbf{s}|$  are the lateral distances from the central axis connecting the centers of the bodies (the integration is over the two-dimensional plane bisecting the two bodies), and  $p_1(s)$  is the local pressure (positive for a repulsion). The quantity on the left-hand side,  $u(r)$ , is the total deformation normal to the surfaces at each position, (negative for flattening). Equation (3.1) shows how the deformation decays away from the point of application of the local stress, and how the total deformation at any point is the linear superposition of the deformation due to these local pressures.

The deformation relates the local nominal separation between the two bodies,  $h_0(r)$ , which would be the separation if the bodies did not deform, to the actual local separation,

$$h(r) = h_0(r) - u(r). \quad (3.2)$$

Here the local separation of the undeformed surfaces is  $h_0(r) = h_0 + r^2/2R$ , where  $h_0$  is the separation on the axis, and where  $R^{-1} = R_1^{-1} + R_2^{-1}$  is the effective radius of the interacting bodies; in general each  $R_i$  is related to the principal radius of curvature of each body [120]. Note that this equation gives the local surface separation, whereas equation (2.3) gives the surface separation on the central axis, which is the point of closest approach of the two bodies.

The oldest theories for the elastic deformation of bodies are contact theories in which the local pressure  $p_1(r)$  is a specified function of radius that when integrated gives  $u(r) = r^2/2R$ , which corresponds to a flat contact region,  $h(r) = 0$ . Hertz theory is applied to repulsive contact, and JKR theory [121] and the theory of Derjaguin, Muller, and Toporov (DMT) [122] are applied to adhesive bodies.

The virtue of contact theories is that they give simple analytic results, but they are unrealistic because the actual interaction force laws between surfaces have an extended range. In these cases the local pressure depends upon the local separation,

$$p_1(r) = p(h(r)), \quad (3.3)$$

where  $p(h)$  is the pressure between two infinite planar walls at a separation of  $h$ , and is given by the van der Waals or electric double layer force law appropriate for the bodies being analyzed. In these so-called soft-contact theories, the local separation depends upon the deformation, and the preceding three equations must be solved by iteration for each nominal separation  $h_0$ . This can be done, and the elastic deformation and adhesion as a function of load for elastic solids interacting with realistic surface forces of extended range have been characterized [76, 77, 81, 123–129].

An efficient algorithm for the solution of the non-contact elastic equation has been given by Attard [76, 128], and it is used for the results presented here. The algorithm self-consistently calculates the surface shape of the elastically deformed bodies due to the local pressure, which, in turn, depends upon the local separation of the deformed bodies. In this way one obtains the actual surface shape and the actual pressure profile, whereas contact

mechanics assumes simplified forms for both. For the present elastic calculations there was no hysteresis between the loading and unloading cycles. (The hysteresis observed in the original papers [76, 77] for soft adhering bodies has since been attributed to a non-equilibrium viscoelastic effect [128, 129].)

**3.1.2. Viscoelastic theory.** The elastic theory becomes inapplicable as the adhesion or deformability of the bodies is increased, because in this regime viscoelastic effects become important. For viscoelastic materials the elasticity parameter in equation (3.1), which gives the instantaneous response to the pressure, is replaced by the creep compliance function, which gives the response to past pressure changes, and this accounts for the prior history of the sample. Hence the generalization of the elastic half-space equation involves a time convolution integral [78, 79],

$$u(r, t) - u(r, t_0) = \int_{t_0}^t dt' \frac{-2}{\pi E(t-t')} \int ds \frac{\dot{p}(h(s, t'))}{|\mathbf{r} - \mathbf{s}|}. \quad (3.4)$$

Here  $\dot{p}(h(r, t))$  is the time rate of change of the local pressure at a distance  $r = |\mathbf{r}|$  from the axis and at time  $t$ . The bodies are assumed stationary up to time  $t_0$ , and, if interacting or in contact, have at that time fixed deformation corresponding to static elastic equilibrium,  $u(r, t_0) = u_\infty(r)$ . This expression is the generalization to interactions of extended range of the contact mechanics expression used by a number of authors [130–133]. In contact mechanics an analytic  $\dot{p}_1(s, t)$  is specified, whereas in the present approach  $\dot{p}(h(s, t))$  is determined self-consistently by the physical force law and the past rate of change of separation.

An algorithm has been developed for solving the viscoelastic problem with arbitrary surface forces of extended range when the creep compliance function is exponential [78],

$$\frac{1}{E(t)} = \frac{1}{E_\infty} + \frac{E_\infty - E_0}{E_\infty E_0} e^{-t/\tau}. \quad (3.5)$$

Here  $E_0$  and  $E_\infty$  are the short- and long-time elasticity parameters, respectively, and  $\tau$  is the relaxation time. This is equivalent to a single relaxation time or simple Kelvin model. The algorithm can be generalized to more complex materials with multiple relaxation times [78]. The present three-parameter model is perhaps the simplest model of viscoelastic materials, and is most applicable at the solid end of the spectrum. An alternative three-parameter expression,  $E(t)^{-1} = C_0 + C_1 t^m$ ,  $0 < m < 1$ , has been used to model liquid-like materials [132–134].

With the exponential creep compliance function, differentiation of the deformation yields [78]

$$\dot{u}(r, t) = \frac{-1}{\tau} [u(r, t) - u_\infty(r, t)] - \frac{2}{\pi E_0} \int ds \frac{\dot{p}(h(s, t))}{|\mathbf{r} - \mathbf{s}|}, \quad (3.6)$$

where  $u_\infty$  is the static deformation that would occur in the limit  $t \rightarrow \infty$  if the pressure profile were fixed at its current value,

$$u_\infty(r, t) = \frac{-2}{\pi E_\infty} \int ds \frac{p(h(s, t))}{|\mathbf{r} - \mathbf{s}|}. \quad (3.7)$$

The rate of change of the pressure is

$$\dot{p}(h(r, t)) = [\dot{h}_0(t) - \dot{u}(r, t)] \left. \frac{dp}{dh} \right|_{h=h(r, t)}, \quad (3.8)$$

where  $\dot{h}_0(t)$  is the specified drive trajectory. Accordingly, equation (3.6) represents a linear integral equation for the rate of change of deformation. It can be solved using the same algorithm that has been developed for the elastic problem [76, 128]. It is then a simple matter to solve the differential equation for the deformation by simple time stepping along the trajectory,  $u(r, t + \Delta t) = u(r, t) + \Delta t \dot{u}(r, t)$ .

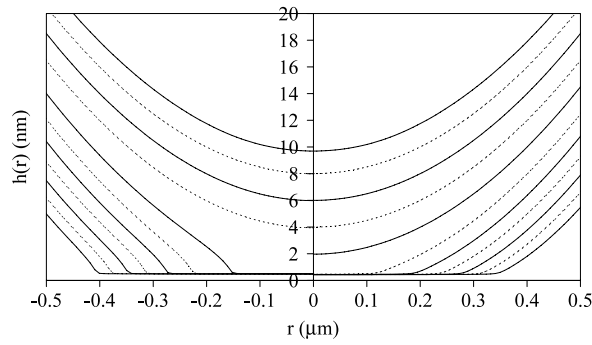


**Figure 8.** Surface profiles for an adhesive elastic sphere interacting with a rigid substrate [76, 106]. The profiles are plotted after every 2 nm drive distance from  $h_0 = 10$  nm (top) to  $-10$  nm (bottom). The Hamaker constant is  $A = 10^{-19}$  J, with  $z_0 = 0.5$  nm and  $R = 10$   $\mu$ m. The right-hand panel is for  $E = 10^{10}$  N m $^{-2}$  and the left-hand panel is for  $E = 10^9$  N m $^{-2}$ .

### 3.2. Attraction and adhesion

The algorithm has been used to obtain results for van der Waals attractions for both elastic [76, 77, 106, 110, 128, 129] and viscoelastic [79, 106, 110] materials. The pressure law used for the van der Waals attraction is

$$p(h) = \frac{A}{6\pi h^3} \left[ \frac{z_0^6}{h^6} - 1 \right], \tag{3.9}$$

where  $A$  is the Hamaker constant, and  $z_0 \approx 0.5$  nm characterizes the length scale of the soft-wall repulsion. The surface energy for comparison with contact theories is given by  $\gamma = A/16\pi z_0^2$ . The calculations are intended as generic examples of viscoelastic behavior, and they model no specific material.

Figure 8 shows the shape of an adhesive elastic sphere during its interaction with a rigid planar substrate for two values of the elasticity parameter that approximately correspond to a rubbery material and to a glass. At the largest separation, where the force is negligible, the surface of the sphere is undeformed. At separations just larger than contact, the surface bulges toward the substrate under the influence of the extended range of the van der Waals attraction. This effect cannot be accounted for by contact theories, and is more pronounced for the softer material. There is a relatively sudden jump into or out of contact, and the lateral radius of the flattened contact region changes most rapidly in the vicinity of the jump. The edges of the contact region are less pronounced for the harder material, but even for the soft material the edge is not infinitely sharp, as JKR theory assumes.

Figure 9 shows a similar calculation for a viscoelastic sphere for approach and retraction, using the same van der Waals attraction as in figure 8. The total time spent on the loading branch is ten times the relaxation time, so that one expects to see viscoelastic effects. The short- and long-time viscoelastic limits used in figure 9 correspond to the two elastic cases treated in figure 8, and one can see similarities in the shapes of the surfaces of the elastic and viscoelastic spheres. In the viscoelastic case of figure 9, one can see the undeformed surfaces at the largest separation prior to approach, the bulge prior to contact, the relatively rapid jump into contact, and initially a fast spreading of the flattened contact region, which continues to grow as the bodies are driven further together. At the edges of the contact region there is a noticeable rounding of the surface profiles on the approach branch. Following the reversal of the motion (unloading) the surfaces become extended as they are pulled apart, and the contact region is more well-defined (there is a sharper transition at the edge) than on the loading branch.

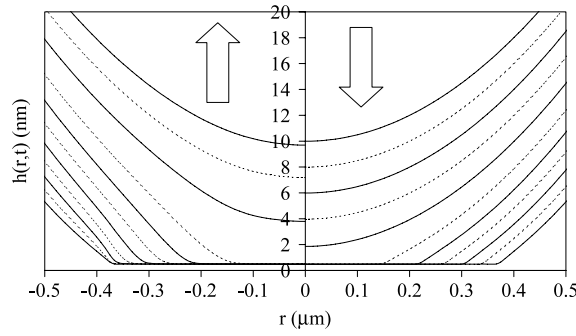


**Figure 9.** Surface profiles for an adhesive viscoelastic sphere approaching toward and then receding from a rigid substrate [79, 106]. The profiles are plotted every millisecond, or every 2 nm from  $h_0 = 10$  nm (top) to  $-10$  nm (bottom). The drive speed is  $|\dot{h}_0| = 2 \mu\text{m s}^{-1}$  and the Hamaker constant is  $A = 10^{-19}$  J, with  $z_0 = 0.5$  nm and  $R = 10 \mu\text{m}$ . The viscoelastic parameters are  $E_0 = 10^{10}$  N m $^{-2}$ ,  $E_\infty = 10^9$  N m $^{-2}$ , and  $\tau = 1$  ms. The right-hand panel is for loading and the left-hand panel is for unloading.

Again it should be noted that even in this case the slopes at the edge of the contact region are not discontinuous as predicted by the JKR theory. Following the turning point, the surfaces appear pinned in contact for a short time before the contact region begins to recede. Due to this extension and stretching, the surfaces remain in contact longer on the unloading branch than on the loading branch. After the surfaces jump apart they retain a memory of the stretching that occurred during unloading, and over times comparable to the relaxation time the local separation is smaller on the unloading branch out of contact than at the corresponding position upon loading.

Figure 10 plots the force against the nominal separation that results from the elastic deformations shown in figure 8. This is what one would measure in an AFM experiment. Most noticeable is the post-contact soft compliance regime, which has a finite slope and is approximately linear at larger loads (see the discussion of photodiode calibration in section 2.1). The negative nominal separations in this regime indicate the amount of flattening of the elastic colloid particle. Prior to contact the attraction is greater than for rigid particles due to the bulging exhibited in the preceding figure. This is clear in figures 10(B) and (C), which test the so-called central deformation approximation [76]. This gives the amount of pre-contact deformation on the axis as a function of the actual separation,

$$u = \frac{A\sqrt{2R}}{8Eh^{5/2}}. \quad (3.10)$$

(Positive deformation corresponds to extension or stretching.) From this one may obtain the nominal separation as a function of the actual separation,  $h_0 = h + u$ , which is tested in figure 10(C). The consequent force is

$$F(h_0) = \frac{-AR}{6h^2}, \quad h_0 = h + \frac{A\sqrt{2R}}{8Eh^{5/2}}. \quad (3.11)$$

It can be seen from figure 10(B) that this simple analytic approximation is quite accurate in the pre-contact regime.

For a viscoelastic sphere, the difference in surface shape on loading and unloading shown in figure 9 gives rise to force hysteresis (figure 11). The hysteresis in the force curves for viscoelastic bodies indicates energy dissipation: the energy required to move the surfaces a nominal distance on loading is not entirely recovered from the system in moving the same

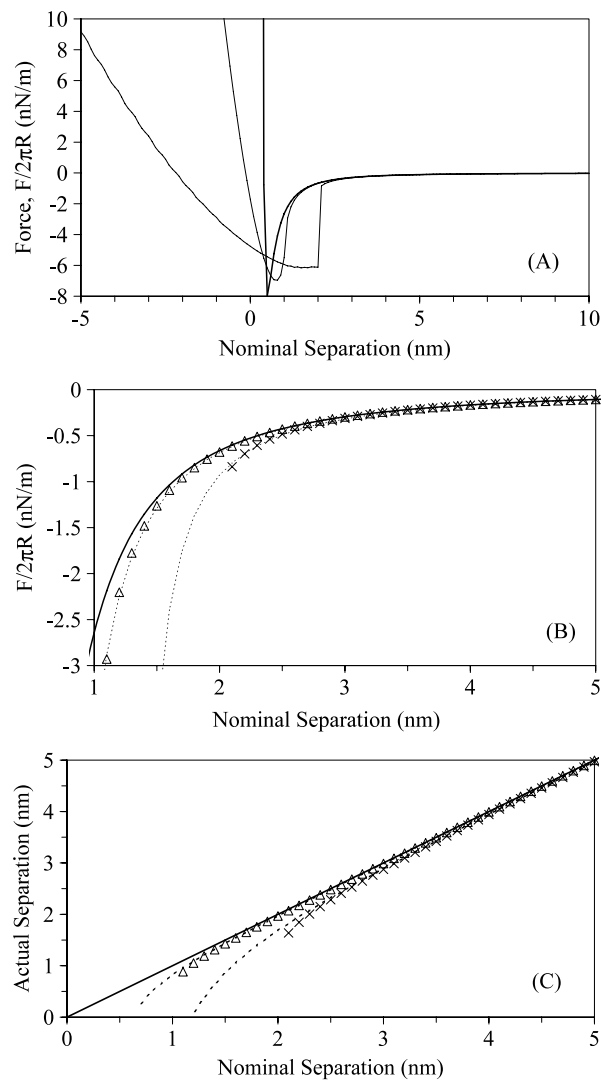


**Figure 10.** Interacting adhesive elastic sphere [76, 106]. (A) Force before and after contact. From left to right in contact the curves are for  $E = 10^9$ , for  $E = 10^{10}$  N m $^{-2}$ , and for a rigid sphere, respectively, with all other parameters as in figure 8. (B) Approaching the elastic jump into contact, the bold line is the rigid sphere, the triangles are for  $E = 10^{10}$  N m $^{-2}$ , and the crosses are for  $E = 10^9$  N m $^{-2}$ . The dotted curves are the central deformation approximation, equation (3.10). (C) Actual surface separation approaching contact, using the same curves and symbols as in part (B).

distance on unloading. The area of the hysteresis loop therefore measures the amount of energy dissipated during the force measurement, and it increases with increasing drive velocity. The physical origin of the decreased repulsion on the unloading curve is that at a given nominal separation the actual local separation is larger on retraction than upon approach (because, as figure 9 reveals, it takes a finite time for the flattened surfaces to relax), and the local pressure and hence the total repulsion is weaker. At slow speeds the viscoelastic curve tends toward the elastic result of figure 10 for the long-time elasticity,  $E = E_\infty$ , and conversely, at high

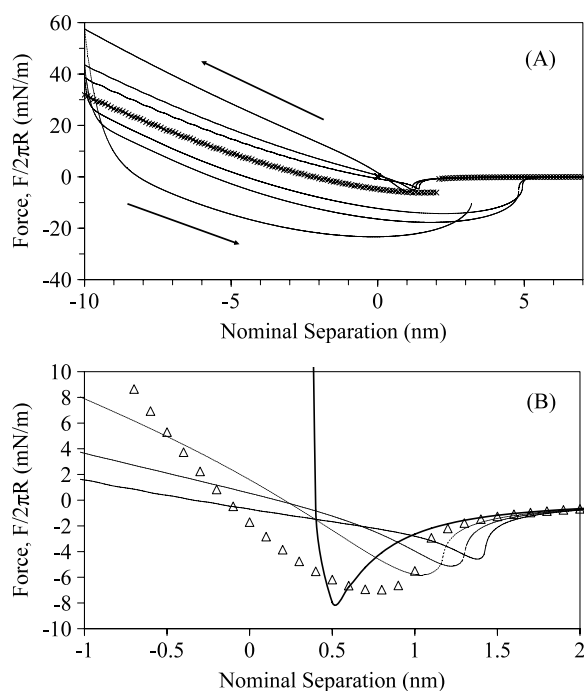


**Figure 11.** Force for an adhering viscoelastic sphere [79, 106]. (A) From inside to outside the hysteresis loops correspond to driving velocities of  $|\dot{h}_0| = 1, 2,$  and  $5 \mu\text{m s}^{-1}$ , using the viscoelastic parameters of figure 9. The crosses represent the static equilibrium elastic result for  $E_\infty = 10^9 \text{ N m}^{-2}$ , (figure 10). (B) Loading curves in the region near initial contact. The triangles represent the static equilibrium elastic result for  $E_0 = 10^{10} \text{ N m}^{-2}$ , and the bold curve is the force for rigid particles.

speeds it tends toward the short-time elastic result,  $E = E_0$  (but only on approach). This is precisely what one would expect from the definitions of the short- and long-time elastic parameters.

The minimum in the force curves in figure 11 increases with increasing velocity. The absolute value of the minimum,  $F^*$ , which is the maximum tension sustained by the bodies, is called the adhesion. It can be seen that the adhesion of the viscoelastic bodies is significantly greater than that of elastic bodies (figure 10). This velocity-dependent adhesion is explored in more detail in figure 12. As the velocity is decreased, the curves asymptote to the static equilibrium elastic result, calculated from equation (3.1). The JKR elastic prediction,  $F^* = 3\pi\gamma R/2$ , is not exact (as a contact approximation it neglects the range of the van der Waals interaction) but is increasingly accurate as the surface energy is increased (equivalently, as the elasticity is decreased). As the velocity increases, and the system is given less time to equilibrate, viscoelastic effects become more evident, and the adhesion increases. Note that the data in figures 11 and 12 were all obtained for the same maximum penetration or indentation,  $\min h_0 = -10 \text{ nm}$ , which is the turn-around point.

### 3.3. Repulsive interaction

In this section results for a viscoelastic sphere interacting with a rigid planar substrate via an electrical double layer repulsion are given. (Analogous results for an elastic sphere were given

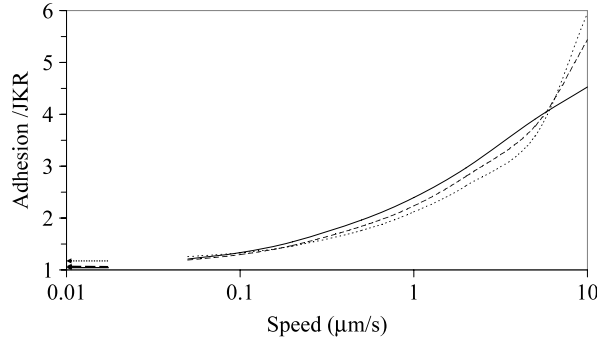


**Figure 12.** Viscoelastic adhesion [79, 106]. The maximum tension (pull-off force,  $F^*$ ) normalized by the JKR elastic adhesion,  $F_{JKR} = 3\pi\gamma R/2$ , is plotted as a function of the drive velocity (logarithmic scale). The parameters are as in figure 9, except that the Hamaker constant is  $A = 1, 5,$  and  $10 \times 10^{-20}$  J (the surface energy is  $\gamma \equiv A/16\pi z_0^2 = 0.80, 3.98,$  and  $7.96$  mJ m $^{-2}$ ), for the dotted, dashed, and solid curves, respectively.

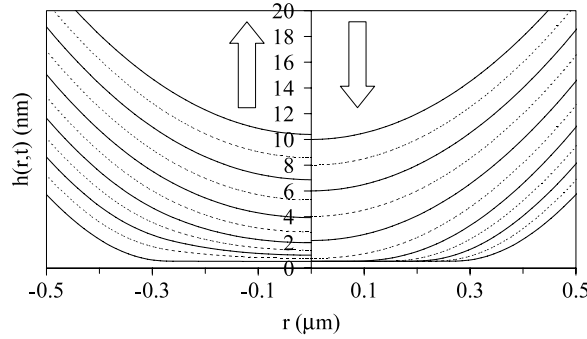


**Figure 13.** Surface profiles for a repulsive viscoelastic sphere approaching toward and then receding from a rigid substrate [78]. The profiles are plotted every 0.4 ms, or every 2 nm from  $h_0 = 10$  nm (top) to  $-10$  nm (bottom). The drive speed is  $|\dot{h}_0| = 5 \mu\text{m s}^{-1}$ . The viscoelastic parameters are  $E_0 = 10^{10}$  N m $^{-2}$ ,  $E_\infty = 10^9$  N m $^{-2}$ , and  $\tau = 1$  ms. The electrical double pressure factor is  $P = 10^7$  N m $^{-2}$ , the decay length is  $\kappa_D^{-1} = 1$  nm, and  $R = 10 \mu\text{m}$ . The right-hand panel is for loading and the left-hand panel is for unloading. The loading profile at  $h_0 = 10$  nm is essentially undeformed.

above in section 2.2.) The pressure between flats that was used was

$$p(h) = Pe^{-\kappa_D h} + P_w(z_0/h)^9, \tag{3.12}$$

where the second term represents a short-ranged repulsion similar to that used in the adhesive case ( $z_0 = 0.5$  nm and  $P_w = P$ ). A Debye length of 1 nm corresponds to 0.1 M monovalent electrolyte, and  $P = 10^7$  N m $^{-2}$  corresponds to a surface potential of 85 mV, which is toward the upper limit encountered in practice.

Figure 13 shows the surface shape for this non-adhesive viscoelastic case. The asymmetry between the loading and unloading surface shapes is due to the finite time over which the measurement is performed. It is clear that on loading the surfaces become relatively flattened, and their shape particularly at the center is largely determined by the geometry and the position rather than by the elastic parameters. Immediately after the turnaround, the flattened regions separate as a whole rather than peeling from the edge, which is what they would do in the elastic case. This is the reason why the contact radius and the force drop so rapidly on the

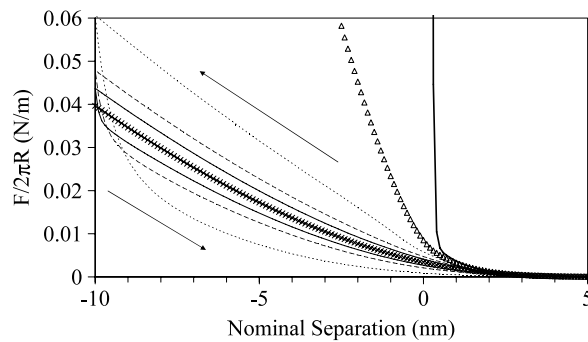


**Figure 14.** Force hysteresis loops for a repulsive viscoelastic sphere [78]. The parameters are as in the preceding figure, with drive velocities of  $\dot{h}_0 = \pm 1, \pm 2,$  and  $\pm 5 \mu\text{m s}^{-1}$ , from inside to outside, respectively. The bold curve is the rigid, undeformable particle result, and the crosses and triangles are the elastic result for  $E = 10^9$  and  $10^{10} \text{N m}^{-2}$ , respectively.

initial part of the unloading branch, as will be seen next. Over the time of unloading the flattened regions relax to their more naturally curved shape. Even though the final unloading profile at  $h_0 = 10 \text{ nm}$  is beyond the range of the surface force, at the high velocity of the figure full relaxation has not yet occurred, and one can see that the surfaces still retain a memory of their contact. The duration of the unloading branch was 2 ms, which is twice the relaxation time,  $\tau = 1 \text{ ms}$ . This remnant flattening means that for a given position the surfaces are at a greater separation on unloading than on loading, and hence the force and the contact area will go rapidly to zero upon unloading.

Figure 14 models typical indentation measurements, which use a triangular drive velocity. Negative values of the position would correspond to interpenetration of the undeformed surfaces, as evinced by the almost vertical force between the rigid particles of the figure as  $h_0 \rightarrow 0^+$ . For deformable surfaces such negative values are allowed and, since the deformation is negative, they correspond to positive actual separations,  $h(r, t) = h_0(r, t) - u(r, t)$ . The force is increasingly repulsive in this regime. What is also noticeable is the hysteresis between the loading and the unloading branches, and the fact that this increases with drive speed. On the loading branch, the force–position curve for the viscoelastic particles lies between the equilibrium elastic results for  $E_\infty$  and for  $E_0$ . Slow driving speeds show a more gradually increasing repulsion and lie closer to the long-term elastic value, as one might expect. As the speed increases the loading curves move towards the equilibrium result for the instantaneous elastic modulus, which has a more sharply increasing repulsion. On the unloading branch, there is initially a rapid decrease in the force immediately following the turning point. This behavior originates in the nature of the change in the surface shape, as was discussed above. Much of the unloading branch lies beneath the static curve corresponding to  $E_\infty$ , and for slow enough driving speed one can well imagine that the two branches will coalesce on it. The fact that the force upon unloading is less than that on loading at a given position gives the appearance that the surfaces come in to contact (i.e. measurably interact) on approach at a greater position than they come out of contact upon retraction, as was discussed in connection with the preceding figure.

Figure 15 shows the pre-contact deformation as the particles are uniformly driven together. The deformation is negative, which corresponds to flattening of the particles under their mutual repulsion. At a given position  $h_0$ , the deformation is greater at the slower driving speed because the soft component of the elasticity has more time to take effect. Conversely and consequently, the force is greater at the faster driving speed because the surface separation of the effectively stiffer material is smaller at a given position (not shown).

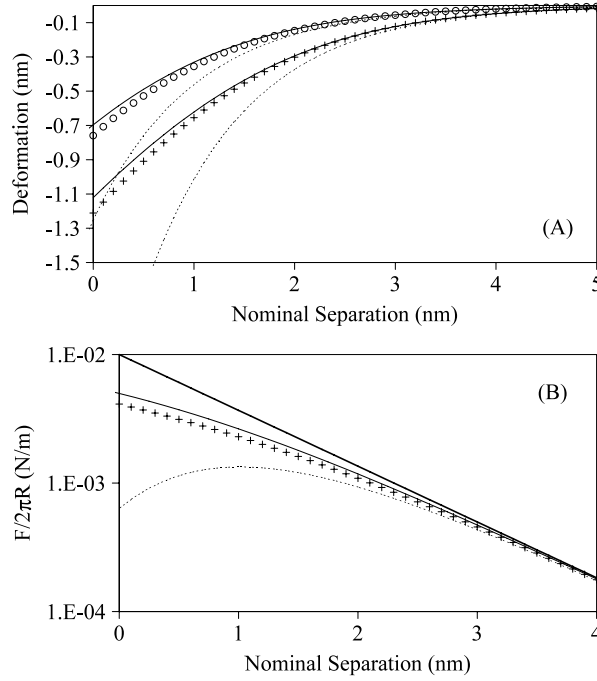


**Figure 15.** Test of the viscoelastic central deformation approximation [78]. The parameters are as in the preceding figure. (A) The drive velocities are  $\dot{h}_0 = \pm 5$  and  $\pm 1 \mu\text{m s}^{-1}$ , for the upper and lower data families, respectively. The symbols represent the exact calculation, the solid curves are the full differential equation, equation (3.13), and the dashed curves are the analytic approximation, equation (3.14). (B) The corresponding forces for  $\dot{h}_0 = \pm 1 \mu\text{m s}^{-1}$ , with the bold line representing the infinitely rigid case (no deformation).

The central deformation approximation replaces the local deformation by that on the central axis  $u(r, t) \Rightarrow u(0, t) \equiv u(t)$ . For a simple pressure law like the present exponential electric double layer repulsion this replacement allows the elastic integral to be evaluated analytically [76, 77]. In the present viscoelastic case it yields [78]

$$\dot{u}(t) = \frac{f(t)\dot{h}_0(t) - [u(t) - u_\infty(t)]/\tau}{1 + f(t)}, \quad (3.13)$$

where  $f(t) \equiv \sqrt{8\pi\kappa_D R P^2 / E_0^2 \exp\{-\kappa_D[h_0(t) - u(t)]\}}$ , and  $u_\infty(t) = -E_0 f(t) / E_\infty \kappa_D$ . For a given trajectory  $h_0(t)$ , the deformation  $u(t)$  is readily obtained from this by simple time stepping.

At large separations  $f(t)$  can be neglected compared to unity in the denominator, and  $\kappa_D u(t)$  can be neglected in the exponent. For a linear trajectory,  $h_0(t) = h_0 + \dot{h}t$ , the solution to the differential equation is

$$u(t) = B[e^{-\kappa_D \dot{h}t} - e^{-t/\tau}], \quad (3.14)$$

where

$$B = \frac{\kappa_D \dot{h} \tau E_0^{-1} - E_\infty^{-1}}{1 - \kappa_D \dot{h} \tau} \sqrt{\frac{8\pi R P^2}{\kappa_D}} e^{-\kappa_D h_0}. \quad (3.15)$$

Since  $\dot{h} < 0$ , one sees that the deformation is negative, which corresponds to flattening. The parameter  $\kappa_D \dot{h} \tau$  controls which of the two values of the elasticity dominate. For materials with

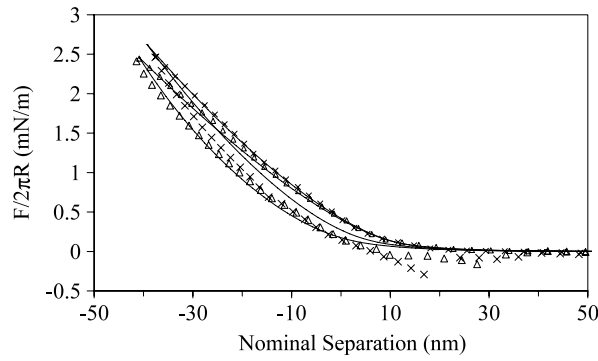


**Figure 16.** AFM measurement of the force between a viscoelastic PDMS droplet ( $R_1 = 0.30 \mu\text{m}$ ) and a silica colloid probe ( $R_2 = 3.5 \mu\text{m}$ ) in 1 mM  $\text{KNO}_3$  at pH 9.3 [83]. The triangles correspond to a drive velocity of  $\dot{h}_0 = \pm 1 \mu\text{m s}^{-1}$  and the crosses to  $\pm 4 \mu\text{m s}^{-1}$ . The curves are the viscoelastic theory using a double layer repulsion with  $P_0 = 4 \times 10^4 \text{ N m}^{-2}$ , ( $\psi_{\text{Si}} = -62 \text{ mV}$  and  $\psi_{\text{PDMS}} = -46 \text{ mV}$ ), plus a short-range steric repulsion and fitted viscoelastic parameters of  $E_0 = 1.2 \times 10^6 \text{ Pa}$ ,  $E_\infty = 0.8 \times 10^6 \text{ Pa}$  and  $\tau = 0.07 \text{ s}$ .

short relaxation times, long-ranged interactions, or for slow driving velocities, this reduces to the static elastic result with  $E = E_\infty$ . In the opposite limit one obtains the static elastic result corresponding to  $E = E_0$ .

For both the full central deformation approximation, equation (3.13), and the approximate central deformation approximation, equation (3.14), the force at a given time is [76–78]

$$F(t) = 2\pi R\kappa_D^{-1} P \exp\{-\kappa_D[h_0(t) - u(t)]\}. \quad (3.16)$$

This result turns out to be the same as the Derjaguin approximation, except that the planar interaction free energy per unit area is calculated at the actual separation  $h(t)$ , as given by the approximation, rather than at the nominal separation  $h_0(t)$ .

As can be seen in figure 15, the central deformation approximation is quite good and it accurately accounts for the viscoelastic behavior prior to contact. The numerical solution of the differential equation, equation (3.13), may be described as quantitatively accurate. The analytic approximation, equation (3.14), works well at large separations but overestimates the deformation closer to contact when  $\kappa_D u(t)$  is no longer negligible.

The actual load at a given position is compared with that for rigid particles in figure 15(B). It can be seen that the requisite load is reduced because the surface separation between deformed particles at a given position is greater than that between undeformed particles. This effect is quite clear in the elastic Derjaguin approximation (equation (3.16)). It may be seen from figure 15(B) that this approximation is quite accurate for the two central varying deformation expressions.

### 3.4. Viscoelastic measurements

Figure 16 shows indentation measurements for a cross-linked PDMS droplet [83]. The photodiode was calibrated and the zero of separation was set as described in section 2. The hysteresis between loading and unloading, and the velocity dependence of the measured force demonstrates that the droplet is viscoelastic. That the droplet appears stiffer when measured at faster speeds (i.e. the force increases more rapidly on approach), is consistent with the theoretical results above. The energy dissipated during the indentation measurement (i.e. the area of the hysteresis loop increases with increasing speed). The data are reasonably well fitted

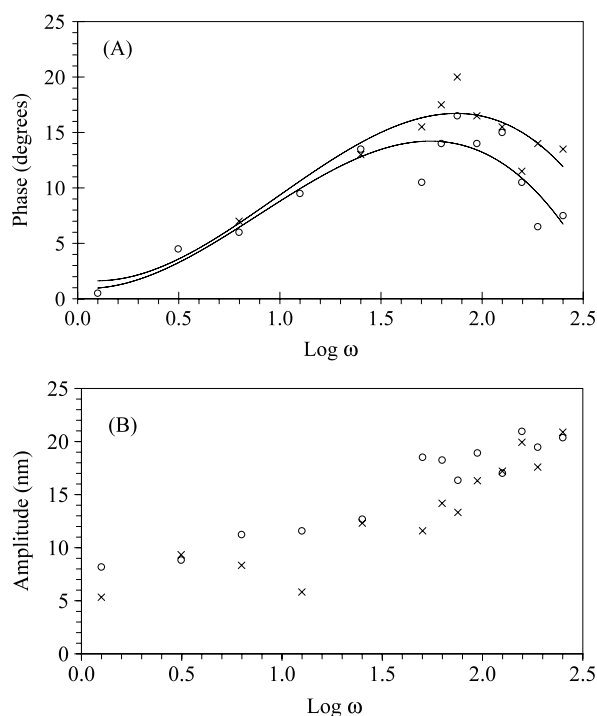


**Figure 17.** Cantilever response for an oscillatory AFM indentation measurement on 4% agar gel in contact [84]. The driving amplitude is 66 nm and the mean load is 14.80  $\mu\text{N}$  (circles) and 9.87  $\mu\text{N}$  (crosses). (A) Phase response. The curves are a third-degree polynomial fit. (B) Amplitude response.

by the viscoelastic theory described above. The theory used an electrical double layer repulsion for the force law. In addition to this, there is evidence of adhesion in the measured data, but this was not taken into account in the theoretical fit. This may contribute to the discrepancy between theory and experiment for the high speed retract data. The fitted elasticities,  $E_\infty = 0.8$  and  $E_0 = 1.2$  MPa, are in agreement with the value of 0.6 MPa measured for cross-linked PDMS by Geneisser *et al* using a rheometer [135]. In the latter measurements the loss modulus significantly increased at about 3 Hz, which is consistent with the timescale of 70 ms given by the theoretical fit in figure 16. Obviously the quantitative results depend upon the amount of cross-linking and the surface versus bulk sensitivity of the measurement method. Nevertheless the data in figure 16 tend to confirm that the AFM in combination with the extended-range viscoelastic theory is capable of quantitatively measuring the material viscoelastic properties.

AFM measurements were also made on agar gel, a soft, biopolymeric solid with high water content [84]. Preliminary exploration established that the material was measurably viscoelastic. A 1 mm thick film of the gel was placed under water in the AFM fluid cell and measurements were performed in contact with a tipped cantilever,  $k = 47 \text{ N m}^{-1}$ . The photodiode was calibrated from the response against a rigid glass slide. For the spectroscopy, the zero of phase lag was similarly established for a rigid substrate. Custom drive signals were generated, and the piezo-drive position, measured with a fibre-optic displacement probe, and photodiode signal, were obtained and stored via a signal access module and digital to analog components of an input and output board [84].

Figure 17 shows the phase and the amplitude response of the cantilever,  $x(t) = A_x \sin(\omega t + \phi)$ , to a sinusoidal piezo-drive,  $z(t) = A_z \sin(\omega t)$ . A positive value of  $\phi$

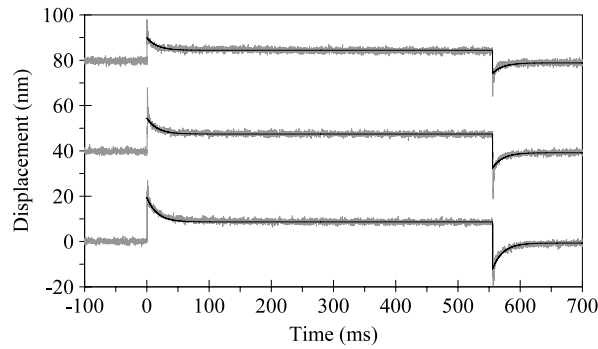


**Figure 18.** Cantilever response for a 66 nm step change the piezo-drive for 4% agar gel in contact [84]. The initial applied loads are 19.74, 9.87, and 4.93  $\mu\text{N}$  from bottom to top, respectively (vertically offset for clarity). A step up in load occurs at  $t = 0$ , and a step back at  $t = 550$  ms. The lines through the measured data are exponential fits using the relaxation time  $\omega_{\text{peak}}^{-1} = 16.6$  ms obtained from the peak of the spectroscopic data.

corresponds to a phase lead. This is indeed what is measured, and at first sight it is a counter-intuitive result. Upon reflection, however, one can see that it is a consequence of the finite relaxation time of the viscoelastic material. The load is increasing at a certain rate, and the deformation is decreasing at the rate of material relaxation. Near the peak of the drive the rate of increase of the load becomes less than the rate of relaxation, so the latter effect dominates, and the change in the response reverses sign before the change in the drive does. This phase lead also occurs in the theoretical results presented below.

The maximum in the phase lead occurs at  $\omega_{\text{peak}} = 60.3 \text{ rad s}^{-1}$ , or 9.6 Hz. At about this frequency there is a step change in the amplitude response (figure 17(B)). The amplitude is smaller at low frequencies than it is at high frequencies, corresponding to the softer nature of the viscoelastic material on long timescales (low frequencies) compared to the short-time response. That is to say,  $E_0 > E_\infty$ .

Figure 18 shows the response to a step change in the piezo-drive. The viscoelastic relaxation of the material is quite clear in the measured data. The exponential relaxation curves have been fitted using a relaxation time equal to the reciprocal of the peak frequency obtained from the spectroscopic data. It can be seen that such a value gives quite a good fit. There is some dependence on load evident in the data.

The spectroscopic and impulse measurements were also modeled using the viscoelastic theory with extended forces described above. Figure 19 shows some typical results. The phase lead seen in the experimental data is confirmed by the theory. The relationship between the relaxation time for the impulse measurement, and the frequency corresponding to the peak phase lead, is also confirmed (not shown). Interestingly enough, this timescale is not equal to the viscoelastic timescale used in the calculations, and in this case one has  $\omega_{\text{peak}} = 0.8\tau$  [84]. The theory predicts that  $\omega_{\text{peak}}$  is independent of the applied load or the cantilever spring constant, (see below).

Let  $x(t)$  be the cantilever deflection at time  $t$  after the step change  $\Delta z$  in the piezo-drive, let  $x(0^-)$  be the static deflection just prior to the step, and let  $r(t) = [x(t) - x(0^-)]/\Delta z$  be the relative change in the deflection. Then the theoretical [78] and the measured AFM data [84] indicate an exponential relaxation of the form

$$r(t) = r_f + [r_i - r_f]e^{-\omega_{\text{peak}}t}, \quad (3.17)$$

where  $r_i = r(0^+)$  is the initial relative deflection immediately after the step and  $r_f = r(t \rightarrow \infty)$  is the final, fully relaxed deflection following the step. For the spectroscopic data, if  $r(\omega) =$

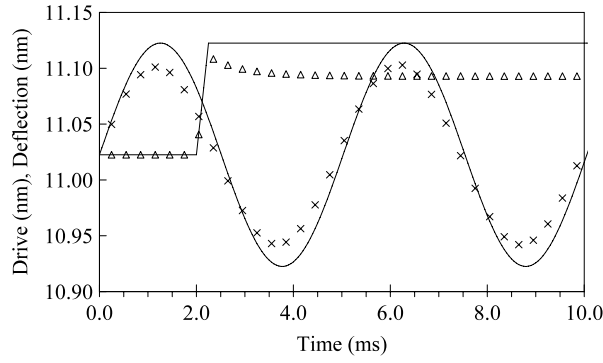


**Figure 19.** Calculated cantilever response (symbols,  $k = 100 \text{ N m}^{-1}$ ) to a step or harmonic piezo-crystal displacement for contact with a viscoelastic material ( $E_0 = 10^{10} \text{ N m}^{-2}$ ,  $E_0 = 10^9 \text{ N m}^{-2}$ ,  $\tau = 1 \text{ ms}$ ), with electrical double layer repulsion ( $P_0 = 10^7 \text{ N m}^{-2}$ ,  $\kappa_D^{-1} = 1 \text{ nm}$ ) plus short-ranged steric repulsion. The radius is  $R = 10 \text{ }\mu\text{m}$ , and the load is  $1.1 \text{ }\mu\text{N}$ . The amplitude is  $0.1 \text{ nm}$  for the step drive, and  $0.2 \text{ nm}$  for the harmonic drive, (curves) [78, 84].

$A_x(\omega)/A_z(\omega)$  is the cantilever amplitude relative to the piezo-drive amplitude, it turns out both theoretically and experimentally that  $r(\omega \rightarrow 0) = r_f$  and  $r(\omega \rightarrow \infty) = r_i$ . The significance of this result is that the three measured parameters,  $r_i$ ,  $r_f$ , and  $\tau$ , may be extracted from either a frequency scan spectroscopic measurement, or from a step measurement. The former is probably easier to automate, and the latter is probably quicker to perform.

Can one extract material properties from rheological measurements? If this is possible, than one ought be able to compare bulk rheological measurements with nanorheological AFM measurements. In macroscopic rheology one defines a rheological phase lag,  $\tan \delta = G''/G'$ , where  $G'$  is the storage modulus and  $G''$  is the loss modulus. The mechanically equivalent quantity for an AFM is [32]

$$\tan \delta = \frac{\sin \phi}{\cos \phi - r(\omega)}. \quad (3.18)$$

The AFM response for this quantity is modeled in figure 20 using the viscoelastic theory with forces of extended range. It can be seen that the magnitude of the rheological phase lag is insensitive to the cantilever spring constant, but quite sensitive to the applied load: decreasing the load by a factor of about five decreases the rheological phase lag by about a factor of two. Conversely, the phase lag itself is insensitive to the load but sensitive to the spring constant. The point is that the instrument compliance and applied stress strongly influences both measures of the phase lag, but in different fashions. What is invariant, however, is the position of the maximum,  $\omega_{\text{peak}}$ .

It should be stressed that the present model is for a linear viscoelastic material, and as such the material parameters cannot change with applied load. However, the instrumental response can and does change with load, as the data in figure 20 indicate.

Figure 21 shows a comparison between macroscopic measurements from a parallel plate rheometer and the AFM measurements. The rheological phase lag is used for comparison purposes. It can be seen that the AFM data are approximately an order of magnitude larger than the macroscopic data. However, as discussed in connection with the preceding figure, the magnitude varies strongly with the applied load, and the local stresses are likely very different in the two measurements. However, the theory predicts that  $\omega_{\text{peak}}$  is a robust quantity, and one can indeed see from figure 21 that the maximum in  $\tan \delta$  occurs at approximately the same frequency in both the macroscopic and the nanoscopic measurement.

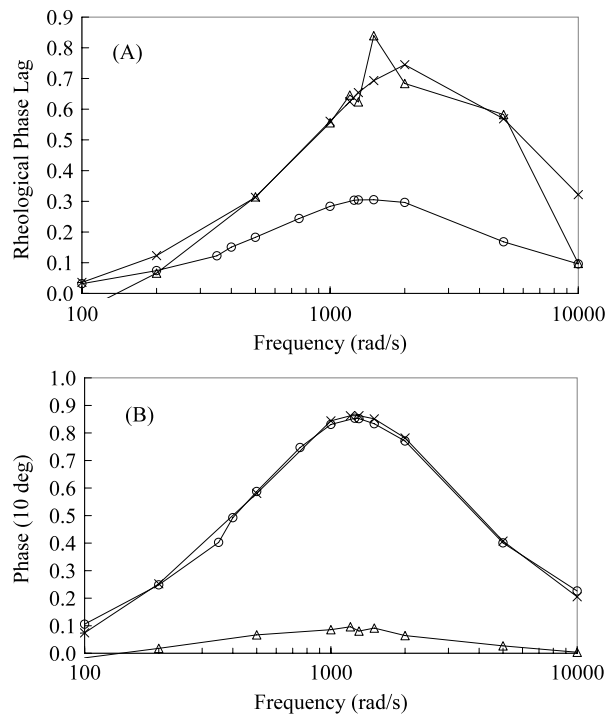


**Figure 20.** Calculated AFM cantilever phase as a function of drive frequency [84]. The triangles correspond to a load of  $L_0 = 1.1 \mu\text{N}$  and  $k = 10 \text{ N m}^{-1}$ , the circles denote  $L_0 = 0.2 \mu\text{N}$  and  $k = 100 \text{ N m}^{-1}$ , and the crosses signify  $L_0 = 1.1 \mu\text{N}$  and  $k = 100 \text{ N m}^{-1}$ . All other parameters are as in figure 19. (A) The rheological phase lag, equation (3.18). (B) The phase lag.

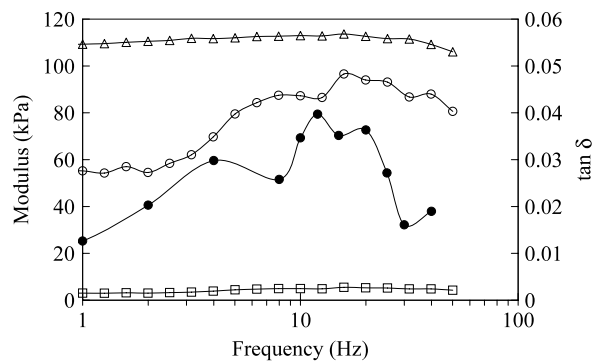


**Figure 21.** Rheometry for 4% agar gel [84]. Open symbols are obtained with a parallel plate laboratory rheometer (frequency sweep at fixed stress of 100 Pa) for the storage modulus  $G'$  (triangles), the loss modulus  $G''$  (squares), and the rheological phase lag  $\tan \delta = G''/G'$  (open circles). The filled circles are  $\tan \delta/10$  for the AFM data, equation (3.18).

#### 4. Conclusion

The AFM has a number of advantages for measuring the properties of elastic and viscoelastic materials. It is a highly localized technique, with sub-micrometer lateral resolution. A number different imaging modes can be used, and these can be correlated with each other to identify

the underlying physical properties of the material. It is a surface sensitive technique, which is essential for characterizing the nature of coatings, membranes, and other laminae, and for elucidating the transition from bulk to interfacial properties.

In order to extract quantitative results from the AFM, attention has to be paid to a number of calibration and measurement issues that arise for deformable surfaces. If the substrate is soft, the photodiode cannot be calibrated from the slope of the contact region, even when the compliance region appears linear. It must be either calibrated against a rigid substrate [91, 106, 110], or else a non-contact thermal method should be used [118]. Whereas the actual surface separation can be obtained for rigid substrates, with zero corresponding to an infinitely steep increase in force, only the nominal separation can be obtained for deformable particles, with negative values corresponding to the amount of flattening. The zero of nominal separation should be determined by a horizontal shift that either sets it at the position following the van der Waals jump into contact [91], or else makes it coincide with the theoretical electric double layer repulsion at large separations, where the deformation is negligible [109]. For viscoelastic measurements, and indeed for reliable force measurements in general, the non-linearity and hysteresis in the piezo-drive must be accounted for. An in-built displacement sensor, closed-loop operation, or an external displacement sensor should be used [84].

With a proper calibration and measurement protocol, the AFM is capable of reliable, quantitative, and very detailed characterization of elastic and viscoelastic properties. The spatial resolution of the probe, when convolved with the slow rate of decay of deformation laterally from the point of application of the stress, is of the order of tens to hundreds of nanometers. The deformation itself (flattening or stretching normal to the surface) can be measured with a distance resolution of the order of a nanometer, and the time resolution can be of the order of a millisecond. In order to exploit the molecular resolution that the AFM is capable of, a similar level of theoretical modeling is required. This in practice means going beyond the usual elastic contact theories and taking into account the extended range of the surface forces. This has been done in for elastic [76, 77] and viscoelastic [78, 79] solids, and for the elastic deformation of gas bubbles and liquid droplets [85, 86]. Quantitative analyses of viscoelastic AFM data have been performed for indentation [83] and for spectroscopic and impulsive [84] measurements.

The extraction of material viscoelastic properties from measurements obtained with macroscopic rheometry are complicated by instrumental compliance, complex geometry, non-uniform loads, and heterogeneous composite materials, and by the lack of surface discrimination and molecular resolution. In contrast the simple mechanical components of the AFM (i.e. cantilever spring, spherical colloid probe, measured piezo-displacement), lend themselves to quite precise modeling such that the instrumental compliance can be fully accounted for. Together with the non-contact theory, this enables the viscoelastic parameters to be reliably extracted and the material properties to be measured with molecular resolution.

## Acknowledgment

The Australian Research Council is thanked for financial support.

## References

- [1] Kajiyama T, Tanaka K, Ohki I, Ge S R, Yoon J S and Takahara A 1994 *Macromolecules* **27** 7932
- [2] Pluta M, Morawiec J, Kryszewski M and Kowalewski T 1996 *J. Therm. Anal.* **46** 1061
- [3] Tamayo J and Garcia R 1996 *Langmuir* **12** 4430
- [4] Bar G, Thomann Y, Brandsch R, Cantow H-J and Whangbo M-H 1997 *Langmuir* **13** 3807

- [5] Bransch R, Bar G and Whangbo M-H 1997 *Langmuir* **13** 6349
- [6] Bar G, Bransch R and Whangbo M-H 1998 *Langmuir* **14** 7343
- [7] Bar G, Ganter M, Bransch R, Delineau L and Whangbo M-H 2000 *Langmuir* **16** 5702
- [8] Cuberes M T, Assender H E, Briggs G A D and Kolosov O V 2000 *J. Phys. D: Appl. Phys.* **33** 2347
- [9] Raghavan D, Vanlandingham M, Gu X and Nguyen T 2000 *Langmuir* **16** 9448
- [10] Dubourg F, Kopp-Marsaudon S, Leclere Ph, Lazzaroni R and Aime P 2001 *Eur. Phys. J. E* **6** 387
- [11] Satomi N, Tanaka K, Takahara A and Kajiyama T 2001 *Macromolecules* **34** 6420
- [12] Scott W W and Bhushan B 2003 *Ultramicroscopy* **97** 151
- [13] Stark R W, Schitter G and Stemmer A 2003 *Phys. Rev. B* **68** 085401
- [14] Bodiguel H, Montes H and Frétigny C 2004 *Rev. Sci. Instrum.* **75** 2529
- [15] Xu W, Wood-Adams P M and Robertson C G 2006 *Polymer* **47** 4798
- [16] Overney R M, Leta D P, Pictroski C F, Rafailovich M H, Liu Y, Quinn J, Sokolov J, Eisenberg A and Overney G 1996 *Phys. Rev. Lett.* **76** 1272
- [17] Dubourg F, Aime J P, Marsaudon S, Boisgard R and Leclere P 2001 *Eur. Phys. J. E* **6** 49
- [18] Radmacher M, Tillmann R W, Fritz M and Gaub H E 1992 *Science* **257** 1900
- [19] Radmacher M 2002 *Methods Cell Biol.* **68** 67
- [20] Mahaffy R E, Shih C K, MacKintosh F C and Käs J 2000 *Phys. Rev. Lett.* **85** 880
- [21] Mahaffy R E, Park S, Gerde E, Käs J and Shih C K 2004 *Biophys. J.* **86** 1777
- [22] Anczykowski B, Krüger D, Babcock K and Fuchs H 1996 *Ultramicroscopy* **66** 251
- [23] Cleveland J P, Anczykowski B, Schmid A E and Elings V B 1998 *Appl. Phys. Lett.* **72** 2613
- [24] Bachelot R, Gleyzes P and Boccara A C 1997 *Probe Microsc.* **1** 89
- [25] Kühle A, Sorensen A H, Zandbergen J B and Bohr J 1998 *Appl. Phys. A* **66** S329
- [26] Fritz M, Radmacher M, Petersen N and Gaub H E 1994 *J. Vac. Sci. Technol. B* **12** 1526
- [27] Haga H, Nagayama M, Kawabata K, Ito E, Ushiki T and Sambongi T 2000 *J. Electron Microsc.* **49** 473
- [28] Charras G T and Horton M A 2002 *Biophys. J.* **82** 2970
- [29] Janovjak H, Müller D J and Humphris A D L 2005 *Biophys. J.* **88** 1423
- [30] Friedenber M C and Mate C M 1996 *Langmuir* **12** 6138
- [31] Tomasetti E, Legras R and Nysten B 1998 *Nanotechnology* **9** 305
- [32] Braithwaite G J C and Luckham P F 1999 *J. Colloid Interface Sci.* **218** 97
- [33] Braithwaite G J C, Luckham P F and Howe A M 1999 *J. Colloid Interface Sci.* **213** 525
- [34] Volodin A, Ahlskog M, Seynaeve E, Van Haesendonck C, Fonseca A and Nagy J B 2000 *Phys. Rev. Lett.* **84** 3342
- [35] Cuenot S, Frétigny C, Demoustier-Champagne S and Nysten B 2003 *J. Appl. Phys.* **93** 5650
- [36] Radmacher M, Tillmann R W and Gaub H E 1993 *Biophys. J.* **64** 735
- [37] Wang L 1998 *Appl. Phys. Lett.* **73** 3781
- [38] San Paulo A and Garcia R 2001 *Phys. Rev. B* **64** 193411
- [39] San Paulo A and Garcia R 2002 *Phys. Rev. B* **66** 041406
- [40] Overney R M, Meyer E, Frommer J, Güntherodt H J, Fujihira M, Takano H and Gotoh Y 1994 *Langmuir* **10** 1281
- [41] Michel D, Kopp-Marsaudon S and Aimé J P 1998 *Tribol. Lett.* **4** 75
- [42] Hammerschmidt J A, Gladfelter W L and Haugstad G 1999 *Macromolecules* **32** 3360
- [43] Meurk A 2000 *Tribol. Lett.* **8** 161
- [44] Basire C and Frétigny C 1999 *Eur. Phys. J. AP* **6** 323
- [45] Basire C and Frétigny C 2001 *Tribol. Lett.* **10** 189
- [46] Roters A and Johannsmann D 1996 *J. Phys.: Condens. Matter* **8** 7561
- [47] Roters A, Gelbert M, Schimmel M, Rühle J and Johannsmann D 1997 *Phys. Rev. E* **56** 3256
- [48] Roters A, Schimmel M, Rühle J and Johannsmann D 1998 *Langmuir* **14** 3999
- [49] Gelbert M, Biesalski M, Rühle J and Johannsmann D 2000 *Langmuir* **16** 5774
- [50] Benmouna F and Johannsmann D 2004 *Langmuir* **20** 188
- [51] Radmacher M, Fritz M, Kacher C M, Cleveland J P and Hansma P K 1996 *Biophys. J.* **70** 556
- [52] Balooch M, Wu-Magidi I C, Balazs A, Lundkvist A S, Marshall S J, Marshall G W, Siekhaus W J and Kinney J H 1998 *J. Biomed. Mater. Res.* **40** 539
- [53] A-Hassan E, Heinz W F, Antonik M D, DCosta N P, Nageswaran S, Schoenenberger C and Hoh J H 1998 *Biophys. J.* **74** 1564
- [54] Goldmann W H, Galneder R, Ludwig M, Xu W M, Adamson E D, Wang N and Ezzell R M 1998 *Exp. Cell Res.* **239** 235
- [55] Lekka M, Laidler P, Gil D, Lekki J, Stachura Z and Hryniewicz A Z 1999 *Eur. Biophys. J.* **28** 312
- [56] Rotsch C, Jacobson K and Radmacher M 1999 *Proc. Natl Acad. Sci. USA* **96** 921

- [57] Canetta E, Duperray A, Leyrat A and Verdier C 2005 *Biorheology* **42** 321
- [58] Darling E M, Zauscher S and Guilak F 2006 *Osteoarthritis Cartilage* **14** 571
- [59] Luckham P F and Maniamaaran S 1997 *Macromolecules* **30** 5025
- [60] Luckham P F 2004 *Adv. Colloid Interface Sci.* **111** 29
- [61] Johnson K L, Kendall K and Roberts A D 1971 *Proc. R. Soc. A* **324** 301
- [62] Chizhik S A, Huang Z, Gorbunov V V, Myshkin N K and Tsukruk V V 1998 *Langmuir* **14** 2606
- [63] Tsukruk V V, Gorbunov V V, Huang Z and Chizhik S A 2000 *Polym. Int.* **49** 441
- [64] Chizhik S A, Gorbunov V V, Fuchigami N, Luzinov I and Tsukruk V V 2001 *Macromol. Symp.* **167** 169
- [65] Tsukruk V V 2003 *Polym. Mater. Sci. Eng.* **88** 528
- [66] Shulha H, Kovalev A, Myshkin N and Tsukruk V V 2004 *Eur. Polym. J.* **40** 949
- [67] Johnson K L 1998 *Microstructure and Microtribology of Polymer Surfaces (ACS Symposium Series vol 741)* ed V V Tsukruk and K Wahl (USA: ACS) p 24
- [68] Vakarelski I U, Toritani A, Nakayama M and Higashitani K 2001 *Langmuir* **17** 4739
- [69] Opdahl A, Kim S H, Koffas T S, Marmo C and Somorjai G A 2003 *J. Biomed. Mater. Res. A* **67A** 350
- [70] Yang G, Rao N, Yin Z and Zhu D M 2006 *J. Colloid Interface Sci.* **297** 104
- [71] Mary P, Chateauinois A and Frétygny C 2006 *J. Phys. D: Appl. Phys.* **39** 3665
- [72] Perriot A and Barthel E 2004 *J. Mater. Res.* **19** 600
- [73] Li J and Chou T-W 1997 *Int. J. Solids Struct.* **34** 4463
- [74] Nogi T and Kato T 1997 *ASME J. Tribol.* **119** 493
- [75] Gacoin E, Frétygny C, Chateauinois A, Perriot A and Barthel E 2006 *Tribol. Lett.* **21** 245
- [76] Attard P and Parker J L 1992 *Phys. Rev. A* **46** 7959
- [77] Parker J L and Attard P 1992 *J. Phys. Chem.* **96** 10398
- [78] Attard P 2001 *Phys. Rev. E* **63** 061604
- [79] Attard P 2001 *Langmuir* **17** 4322
- [80] Attard P, Schulz J and Rutland M W 1998 *Rev. Sci. Instrum.* **69** 3852
- [81] Feiler A, Larson I, Jenkins P and Attard P 2000 *Langmuir* **16** 10269
- [82] Attard P and Parker J L 1992 *J. Phys. Chem.* **96** 5086
- [83] Gillies G S, Prestidge C A and Attard P 2002 *Langmuir* **18** 1674
- [84] Tyrrell J W G and Attard P 2003 *Langmuir* **19** 5254
- [85] Attard P and Miklavcic S J 2001 *Langmuir* **17** 8217
- [86] Attard P and Miklavcic S J 2002 *J. Colloid Interface Sci.* **247** 255
- [87] Ducker W A, Senden T J and Pashley R M 1991 *Nature* **353** 239
- [88] Cleveland J P, Manne S, Bocek D and Hansma P K 1993 *Rev. Sci. Instrum.* **64** 403
- [89] Senden T J and Ducker W A 1994 *Langmuir* **10** 1003
- [90] Neumeister J M and Ducker W A 1994 *Rev. Sci. Instrum.* **65** 2527
- [91] Rutland M W, Tyrrell J W G and Attard P 2004 *J. Adhes. Sci. Technol.* **18** 1199
- [92] Feiler A, Attard P and Larson I 2000 *Rev. Sci. Instrum.* **71** 2746
- [93] Hunter R J 1986 *Foundations of Colloid Science* vol 1 (Oxford: Oxford University Press)
- [94] Akeland D R 1996 *The Science and Engineering of Materials* 3rd edn (London: Chapman and Hall)
- [95] Meyers G F, DeKoven B M and Seitz J T 1992 *Langmuir* **8** 2330
- [96] Keddie J L, Jones R A L and Cory R A 1994 *Europhys. Lett.* **27** 59
- [97] Kajiyama T, Tanaka K and Takahara A 1995 *Macromolecules* **28** 3482
- [98] Kajiyama T, Tanaka K and Takahara A 1997 *Macromolecules* **30** 280
- [99] Forrest J A and Dalnoki-Veress K 2001 *Adv. Colloid Interface Sci.* **94** 167
- [100] Teichroeb J H and Forrest J A 2003 *Phys. Rev. Lett.* **91** 016104
- [101] Attard P, Pettersson T and Rutland M W 2006 *Rev. Sci. Instrum.* **77** 116110
- [102] Higgins M J, Proksch R, Sader J E, Polcik M, Mc Endoo S, Cleveland J P and Jarvis S P 2006 *Rev. Sci. Instrum.* **77** 013701
- [103] Martin Y, Williams C C and Wickramasinghe H K 1987 *J. Appl. Phys.* **61** 4723
- [104] Hutter J L and Bechhoefer J 1993 *Rev. Sci. Instrum.* **64** 1868
- [105] Sader J E, Larson I, Mulvaney P and White L R 1995 *Rev. Sci. Instrum.* **66** 3789
- [106] Attard P and Gillies G 2001 *Aust. J. Chem.* **54** 477
- [107] Attard P 1993 *Phys. Rev. E* **48** 3604
- [108] Attard P, Antelmi D and Larson I 2000 *Langmuir* **16** 1542
- [109] Gillies G S, Prestidge C A and Attard P 2001 *Langmuir* **17** 7955
- [110] Attard P 2002 *J. Adhes. Sci. Technol.* **16** 753
- [111] Hartley P G, Grieser F, Mulvaney P and Stevens G W 1999 *Langmuir* **15** 7282
- [112] Hartley P G, Larson I and Scales P J 1997 *Langmuir* **13** 2207

- [113] Nespolo S A, Bevan M A, Chan D Y C, Grieser F and Stevens G W 2001 *Langmuir* **17** 7210
- [114] Attard P and Miklavcic S J 2003 *Langmuir* **19** 2532
- [115] Hoh J H and Engel A 1993 *Langmuir* **9** 3310
- [116] Attard P, Carambassis A and Rutland M W 1999 *Langmuir* **15** 553
- [117] Stiernstedt J, Rutland M W and Attard P 2005 *Rev. Sci. Instrum.* **76** 083710
- [118] Attard P, Stiernstedt J and Rutland M W 2007 *J. Phys.: Conf. Ser.* **61** 51
- [119] Landau L D and Lifshitz E M 1970 *Theory of Elasticity* 2nd English edn (London: Pergamon)
- [120] White L R 1983 *J. Colloid Interface Sci.* **95** 286
- [121] Johnson K L, Kendall K and Roberts A D 1971 *Proc. R. Soc. A* **324** 301
- [122] Derjaguin B V, Muller V M and Toporov Yu 1975 *J. Colloid Interface Sci.* **53** 314
- [123] Muller V M, Yushchenko V S and Derjaguin B V 1980 *J. Colloid Interface Sci.* **77** 91
- [124] Hughes B D and White L R 1979 *Q. J. Mech. Appl. Math.* **32** 445
- [125] Pethica J B and Sutton A P 1988 *J. Vac. Sci. Technol. A* **6** 2490
- [126] Smith J R, Bozzolo G, Banerjee A and Ferrante J 1989 *Phys. Rev. Lett.* **63** 1269
- [127] Greenwood J A 1997 *Proc. R. Soc. A* **453** 1277
- [128] Attard P 2000 *J. Phys. Chem. B* **104** 10635
- [129] Attard P 2001 *Phys. Rev. E* **63** 011601
- [130] Yang W H 1966 *J. Appl. Mech.* **33** 395
- [131] Ting T C T 1968 *J. Appl. Mech.* **35** 248
- [132] Hui C-Y, Baney J M and Kramer E J 1998 *Langmuir* **14** 6570
- [133] Lin Y Y, Hui C-Y and Baney J M 1999 *J. Phys. D: Appl. Phys.* **32** 2250
- [134] Schapery R A 1989 *Int. J. Fract.* **39** 163
- [135] Geneisser L H, Hendriks K C P, Baaijens F T P and Meijer H E H 2000 *J. Rheol.* **44** 1003